

IAPv4 ocean temperature and ocean heat content gridded dataset

Lijing Cheng^{1,11*}, Yuying Pan^{1,11}, Zhetao Tan^{1,11}, Huayi Zheng^{1,11}, Yujing Zhu^{1,11}, Wangxu Wei^{1,11}, Juan Du¹, Huifeng Yuan^{2,11}, Guancheng Li³, Hanlin Ye¹, Viktor Gouretski¹, Yuanlong Li^{4,11}, Kevin E. Trenberth^{5,6}, John Abraham⁷, Yuchun Jin^{4,11}, Franco Reseghetti⁸, Xiaopei Lin⁹, Bing Zhang^{4,11}, Gengxin Chen^{10,11}, Michael E. Mann¹², Jiang Zhu^{1,11}

¹ Institute of Atmospheric Physics, Chinese Academy of Sciences, Beijing, China, 100029.

² Computer Network Information Center, Chinese Academy of Sciences, Beijing, 100083.

³ Eco-Environmental Monitoring and Research Center, Pearl River Valley and South China Sea Ecology and Environment Administration, Ministry of Ecology and Environment, PRC, Guangzhou 510611, China.

⁴ Institute of Oceanography, Chinese Academy of Sciences, Qingdao, China.

⁵ National Center for Atmospheric Research, PO Box 3000, Boulder, CO 80307, USA.

⁶ University of Auckland, Auckland, New Zealand.

⁷ University of St. Thomas, School of Engineering, 2115 Summit Ave., St Paul, MN 55105, USA.

⁸ [Istituto Nazionale di Geofisica e Vulcanologia, 40127, Bologna, Italy.](#)

⁹ Frontier Science Center for Deep Ocean Multispheres and Earth System and Physical Oceanography Laboratory, Ocean University of China, Qingdao, China.

¹⁰ State Key Laboratory of Tropical Oceanography, South China Sea Institute of Oceanology, Chinese Academy of Sciences, Guangzhou, China

¹¹ University of Chinese Academy of Sciences, Beijing, China.

¹² Dept. of Earth and Environmental Science, University of Pennsylvania, Philadelphia PA, USA

Correspondence to: Lijing Cheng (chenglij@mail.iap.ac.cn)

删除了: Italian National Agency for New Technologies, Energy and Sustainable Economic Development, S. Teresa Research Center

删除了: Lericci 19032

设置了格式: 字体: (默认) Times New Roman, 12 磅

33 **Abstract.** Ocean observational gridded products are vital for climate monitoring, ocean
34 and climate research, model evaluation, and supporting climate mitigation and adaptation
35 measures. This paper describes the 4th version of the Institute of Atmospheric Physics
36 (IAPv4) ocean temperature and ocean heat content (OHC) objective analysis product. It
37 accounts for recent developments in quality control (QC) procedures, climatology, bias
38 correction, vertical and horizontal interpolation, and mapping and is available for the upper
39 6000 m (119 levels) since 1940 (more reliable after ~1957) for monthly and 1° × 1°
40 temporal and spatial resolutions. The IAPv4 is compared with the previous version, IAPv3,
41 and to the other data products, sea surface temperatures (SSTs), and satellite observations.
42 It has a slightly stronger long-term upper 2000 m OHC increase than IAPv3 for 1955-
43 2023, mainly because of newly developed bias corrections. IAPv4 OHC 0-2000 m trend is
44 also higher during 2005-2023 than IAPv3. The **uppermost** level of IAPv4 is consistent with
45 independent SST datasets. The month-to-month OHC variability for IAPv4 is desirably
46 less than IAPv3 and other OHC products investigated in this study, **the trend of ocean**
47 **warming rate (i.e., warming acceleration) is more** consistent with the net energy imbalance
48 at the top of the atmosphere **than IAPv3**, and the sea level budget can be closed within
49 uncertainty. The gridded product is freely accessible at:
50 <http://dx.doi.org/10.12157/IOCAS.20240117.002> for temperature data (Cheng et al.,
51 [2024a](http://dx.doi.org/10.12157/IOCAS.20240117.001)) and <http://dx.doi.org/10.12157/IOCAS.20240117.001> for ocean heat content data
52 (Cheng et al., 2024b).

53

54 1. Introduction

55 Observational gridded products are essential for understanding the ocean, the
56 atmosphere, and climate change; they support policy decisions and social-economy
57 developments (Abraham et al., 2022; Abraham and Cheng, 2022; Cheng et al., 2022a). For
58 instance, many of the climate indicators used in the Working Group I report of the 6th
59 Intergovernmental Panel on Climate Change (IPCC-AR6-WG1) are **based on** gridded
60 products (Gulev et al., 2021; IPCC, 2021), mainly because the raw oceanic data suffer
61 from inhomogeneous data quality and irregular and incomplete data coverage (Abraham et
62 al., 2013; **Boyer et al., 2016**; Cheng et al., 2022a; Meyssignac et al., 2019).

删除了: first

删除了: ;

删除了: annual variations

删除了: are

67 As more than 90% of the Earth's energy imbalance (EEI) in the past half-century has
68 accumulated in the ocean, increasing ocean temperature (T) and ocean heat content (OHC)
69 are essential climate variables for monitoring, understanding, and projecting climate
70 change (e.g., Rhein et al., 2013; Hansen et al., 2011; Trenberth, 2022; Trenberth et al.,
71 2009; von Schuckmann et al., 2020; Cheng et al., 2022). OHC also impacts air-sea and ice-
72 sea interactions and thus exerts a considerable influence over the other components of the
73 climate system. It provides critical feedback through energy, water, and carbon cycles
74 (Cheng et al., 2022a; Trenberth, 2022; von Schuckmann et al., 2016). Substantial changes
75 in ocean temperatures also profoundly impact ocean biogeochemical processes and
76 ecosystems and are critical for ocean health and human society (Bindoff et al., 2019;
77 Cheng et al., 2022a).

78 Many gridded T/OHC datasets have been produced by independent groups, and most
79 of them are updated annually or more frequently (Cheng et al., 2022a; Good et al., 2013;
80 Hosoda et al., 2008; Ishii et al., 2017; Levitus et al., 2012; Li et al., 2017; Meyssignac et
81 al., 2019; Roemmich and Gilson, 2009). Most widely-used products are at $1^\circ \times 1^\circ$
82 horizontal resolution and monthly temporal resolution from near-surface to at least 2000 m
83 depth. Some products utilize all available *in situ* observations and span at least half a
84 century, prominent examples being the data products compiled by the Institute of
85 Atmospheric Physics (IAP) (Cheng and Zhu, 2016; Cheng et al., 2017) from 1940-present;
86 Japan Meteorological Agency (JMA) (Ishii et al., 2017) from 1955-present; National
87 Centers for Environmental Information (NCEI), National Oceanic and Atmospheric
88 Administration (NOAA) from 1950-present (Levitus et al., 2012); and University of
89 California since 1949 (Bagnell and DeVries, 2021). As Argo data has achieved near-global
90 upper 2000 m open ocean coverage since ~2005, many Argo-based or Argo-only gridded
91 products are available. Examples include gridded products from SCRIPPS after 2004
92 (Roemmich and Gilson, 2009); China Argo Real-time Data Center since 2005 (Li et al.,
93 2017); and Copernicus since 2005 (von Schuckmann and Le Traon, 2011). These products
94 usually span from ~2005 to the present for the upper ~2000 m. These data benefit from the
95 high quality of Argo data but are not fully resolving polar regions, shallow waters, and
96 regions with complex topography.

97 In 2016, the IAP group provided its first gridded product for the upper 700 m ocean
98 (Cheng and Zhu, 2016) by merging all available observations since 1960. With a revised
99 mapping method and a thorough evaluation process with synthetic observations, an update

100 (IAP version 3, IAPv3) became available in 2017 for the upper 2000 m ocean with data
101 since the 1950s (Cheng et al., 2017). The IAPv3 has supported scientific research, climate
102 assessment reports, and monitoring practices (Bindoff et al., 2019; Gulev et al., 2021;
103 WMO, 2022).

104 After the release of IAPv3, there has been progress with observation data quality
105 control and new/updated techniques for temperature data processing and reconstruction.
106 For example, Gouretski et al. (2022) found that old Nansen cast bottle data contained
107 systematic biases that impacted the T/OHC data before 1990. Revisions are also available
108 to the bias corrections for the Mechanical Bathythermographs (MBT) and eXpendable
109 Bathythermographs (XBT) data (Cheng et al., 2014; Gouretski and Cheng, 2020), mainly
110 impacting the data within 1940–2005. Tan et al. (2023) developed a new quality-control
111 system that advances the detection of outliers after accounting for the non-Gaussian
112 distribution of local temperatures in determining the local climatological range. The impact
113 of inhomogeneous vertical resolution of temperature profiles has been recognized
114 previously (Cheng and Zhu, 2014) and received more attention recently (Li et al., 2020)
115 with a new vertical interpolation approach (Barker and McDougall, 2020). Upgrading the
116 product with new developments is important to better support the ocean/climate research
117 and climate assessments.

删除了: follow-on

删除了: studies

删除了: on

118 This manuscript discusses the revisions to the IAP ocean objective analysis product
119 (IAPv4) since the publication of the IAPv3 (Cheng et al., 2017). The data and methods are
120 introduced in Section 2 and the results are presented in Section 3, with analyses of the
121 character of the IAPv4 on regional and global scales and at various time scales. The EEI
122 and sea level budgets based on the new data product are also investigated. A summary and
123 discussion are provided in Section 4, with some remaining issues and outlooks being
124 discussed.

125

126 **2. Data and Methods**

127 **2.1 Data source**

128 The majority of the *in situ* measurements used to create the data product come from
129 the World Ocean Database (WOD), downloaded in September 2023. Data from all
130 instrument types are used, including XBTs (Goni et al., 2019), Argo (Argo 2000),
131 Conductivity/Temperature/Depth profilers (CTDs), MBTs, bottles, moorings, gliders,
132 Animal Borne Ocean Sensors (McMahon et al., 2021) and others (Boyer et al., 2018) (Fig.

136 1). There is a total of 17,634,865 temperature profiles from January 1940 to September
137 2023 (Fig. 1a). MBT, XBT, Nansen Bottle and CTD data are the major instruments before
138 2000 (Fig. 1a, b). The spatial coverage of these data increased to >30% in 1960 and >70%
139 in the late 1960s for $1^\circ \times 1^\circ \times 1$ -year resolution. After 2005, there is a huge number of
140 GLD and APB data, and as they are mainly distributed in the polar regions (APB) and
141 coastal regions (GLD) (Fig. 1a), their spatial coverage is usually less than 5% for $1^\circ \times 1^\circ \times$
142 1 year resolution. By contrast, the Argo data cover most of the global open ocean since
143 ~2005 (Fig. 1b).

删除了: thus

删除了: s

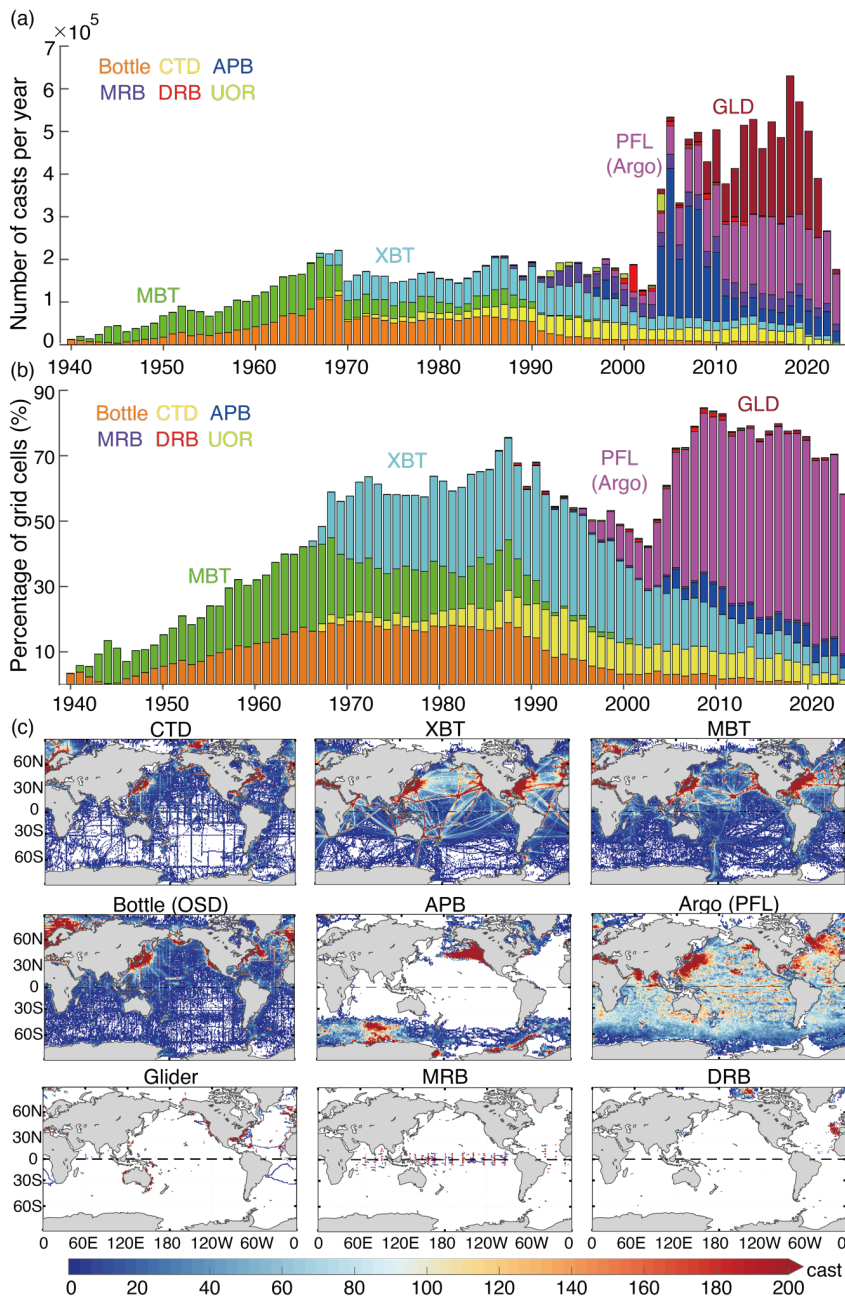
144 Argo data are processed following the recommendations of the Argo community.
145 Adjusted data are used where applicable. Both Delayed- and Real-Time Argo data have
146 been incorporated in IAPv4. As Real-Time Argo data have only passed automated, simple
147 QC tests in real-time, these data may still contain temperature, pressure, and salinity values
148 affected by unknown errors. However, through a sensitivity study, Cheng (2024) indicated
149 that including Real-Time Argo data does not bias the OHC calculation for the IAP
150 analysis. Nevertheless, IAP data are updated frequently (every 1-3 months): each time the
151 updated Argo data is used, the T/OHC fields are recalculated following the
152 recommendation by the Argo group (Wong et al., 2020). The data from the Argo floats in
153 the “grey list” have been removed from the calculation (<https://data-argo.ifremer.fr/>).

154 To complement the WOD with relatively less data in the Arctic and coastal regions of
155 the Northwest Pacific, this presented product also uses data from other sources. The
156 majority of these data are from the Chinese Academy of Sciences Ocean Science Data
157 Center (Zhang et al., 2024), and some data are rescued from the old documents of marine
158 surveys. All these data will be publicly available. There are a total of 85,990 additional
159 temperature profiles, about 0.50% of the data, which is expected to improve the
160 reconstruction in these data-sparse regions (compared with IAPv3 and other products).

删除了: paper

161 The *in situ* data have been processed as described in a flow chart in Figure 2. In the
162 following sections, the key techniques of data processing are introduced.

163



194 estimates has not been evaluated in previous community-assessments on T/OHC
195 uncertainty (Boyer et al., 2016; Lyman et al., 2010). In this study, the QC procedure
196 follows the CAS-Ocean Data Center (CODC) Quality Control system, named CODC-QC
197 (Tan et al., 2023), where only the “good” data (flag=0) are used.

198 The CODC-QC system (Tan et al., 2023) has the following strengths, which make it
199 particularly suitable for T/OHC reconstruction:

200 1) A new local climatological range is defined in this CODC-QC system to identify
201 the outliers. Unlike many existing QC procedures, no assumption is made of a Gaussian
202 distribution law in the new approach, as the oceanic variables (e.g., temperature and
203 salinity) are typically skewed. Instead, the 0.5 % and 99.5 % quantiles are used as
204 thresholds in CODC-QC to define the local climatological parameter ranges.

205 2) Local climatological ranges change with time to account for the long-term trends of
206 ocean temperature accompanied by more frequent extreme events (e.g., [Oliver et al., 2018](#);
207 [Sun et al., 2023](#)). Previously, the use of the static local ranges tended to remove too many
208 “extreme values” (at the tails of the temperature distributions) associated with climate
209 change in recent years that were actually real, leading to a QC-procedure related bias in the
210 gridded dataset and OHC estimate (Tan et al., 2023).

211 3) In addition, local climatological ranges for the vertical temperature gradient are
212 constructed to account for the variability of ‘vertical shape’, increasing the ability of the
213 scheme to identify spurious profiles.

214 4) The QC procedure is instrument-specific, accounting for characteristics inherent to
215 particular instrumentation types. For example, XBT digital recording systems are allowed
216 to continue to record beyond the rated terminal depth suggested by manufacturers (T7/DB
217 probes below 760 m; T4/T6 below 460 m; T5 below 1830 m). Below the rated maximum
218 depth, the XBT wire often breaks, leading to a characteristic change in recorded
219 temperature values. The new QC procedure effectively identifies such profiles.

220 5) The thorough evaluation of the QC procedure performance and the application of
221 the QC procedure to the manually QC-ed datasets ([Thresher et al., 2008](#); [Gouretski and
222 Koltermann, 2004](#)) demonstrated the effectiveness of the proposed scheme in removing
223 spurious data and minimizing the percentage of mistakenly flagged good data.

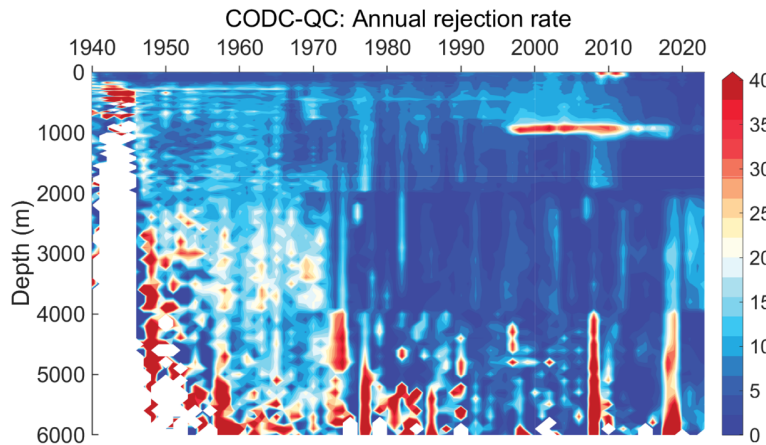
224 Being applied to the entire temperature profile dataset the CODC-QC procedure
225 identifies 6.22 % of all temperature measurements as outliers. The rejection rates
226 (definition follows Tan et al., 2023) vary among instrumentation types (3.73 % for CTD,

删除了: events

228 1.97 % for Argo, 12.06 % for XBT, 4.93 % for MBT, 6.54 % for bottle, 5.92 % for APB,
 229 4.54 % for DRB, 2.55 % for MRB). The overall percentage of outliers decreases over time
 230 from ~5 % in the 1940s to ~2.5 % in the 2020s, reflecting the progressive improvement of
 231 the instrumentation (Fig. 3). A rejection rate maximum (~12 %) during 2000~2010 is
 232 linked to the XBT data, which are especially abundant in the 800–1100m layer and are
 233 characterized by higher rejection rate below the maximum depth (Tan et al., 2023). The
 234 generally higher rejection rate below 4000 meters is related to the gross errors (such as
 235 measurements cooler than -2°C, big spikes, etc.) and the occurrence of the constant values
 236 (recorded values don't change with depth). For example, the higher rejection rate within
 237 2008-2009 below 4000 meters is because of the gross errors in the CTD data.

删除了： 2010

删除了： glider



238
 239 **Figure 3: The rejection rate (%) after CODC-QC as a function of calendar year and**
 240 **depth.**

241
 242 **2.3 Bias correction**

243 It is well known that data from several instrument types can exhibit biases both in
 244 temperature and depth. Temperature profiles obtained using XBTs and MBTs provide an
 245 example of biased data, especially because of uncertainties in the depth of measurement.
 246 Gouretski and Koltermann (2007) demonstrated their significant impact on the magnitude
 247 and variability of the global OHC estimates. That study triggered a series of publications
 248 where different bias correction schemes have been suggested for XBT (Gouretski and

251 Reseghetti, 2010; Abraham et al., 2013; Cheng et al., 2016; Levitus et al., 2009; Wijffels et
252 al., 2008), MBT (Gouretski and Cheng 2020; Levitus et al., 2009) and other instruments
253 (Fig. 2). In the compilation of IAPv4, newly developed bias correction schemes are
254 applied.

255 The XBT temperature bias was found to be **generally positive**, as large as ~ 0.1 °C
256 before 1980 on the global 0–700 m average, diminishing to less than 0.05 °C after 1990
257 (Gouretski and Koltermann 2007; Wijffels et al., 2008). Here, we use an updated XBT bias
258 correction scheme (Cheng et al., 2014) to correct both depth and temperature biases in
259 XBT data, following the community recommendation (Cheng et al., 2016; Goni et al.,
260 2019). The depth and temperature biases depend on ocean temperature, probe type, and
261 time. An inter-comparison among several correction schemes rated the CH14 scheme the
262 most successful (Cheng et al., 2018). Using XBT and collocated CTD data, we updated the
263 CH14 scheme by re-calculating bias corrections between 1966–2016 and extending them
264 for the years 2017 to 2023.

265 Comparison with collocated reference CTD profiles recently revealed significant
266 **biases** in the old hydrographic profiles obtained by means of Nansen bottle casts
267 (Gouretski et al., 2022). Both depth and temperature measurements of bottle casts were
268 found to be biased, and the proposed correction scheme was also implemented in IAPv4.
269 The thermal bias is related to the time needed to bring the mercury thermometers in
270 equilibrium with the ambient temperature after the completion of the hydrographic cast.
271 The depth bias indicates an overestimation of the bottle depth due to the wire's deviation
272 from the vertical position and is mostly related to the hydrographic casts where the
273 thermometrical method of sample depth determination was not used. The correction
274 scheme includes a constant thermal bias of -0.02 °C and a depth- and time-variable depth
275 bias.

276 The MBT bias is as large as 0.28 °C before 1980 for the global average and reduces to
277 less than 0.18 °C after 1980 for the 0–200 m average. IAPv3 used **Ishii and Kimoto, (2009)**
278 (IK09) scheme to correct MBT bias, while a new scheme proposed by **Gouretski and**
279 **Cheng, (2020)** (GC20) is adopted in IAPv4. This shift is made because our assessment
280 indicates the under-correction of MBT bias by the IK09 scheme within the upper 120 m
281 and over-correction in the deeper layer, whereas GC20 corrects both depth and temperature
282 biases. GC20 also found the MBT bias to be country-dependent, explained in terms of
283 different instrumentation characteristics and working procedures. Therefore, the time-

删除了: systematic biases

删除了: (

删除了: (

287 varying bias corrections are applied separately for the MBT profiles obtained by ships
288 from the United States, Soviet Union/Russia, Japan, Canada, and Great Britain. Data from
289 all other countries are corrected using a globally averaged correction.

290 Finally, thermal biases were recently reported for the data obtained by different kinds
291 of data loggers attached to marine mammals (APB). Gouretski et al. (2024) analysed
292 temperature profiles obtained between 2004 and 2019 in the high and moderate latitudes of
293 both hemispheres. Comparison with the collocated reference CTD and Argo float data
294 revealed a systematic negative thermal offset (average value $-0.027\text{ }^{\circ}\text{C}$) for mammal
295 temperature profiles from SRDL (satellite-related data loggers). For the less accurate data
296 from TDR (Temperature-Depth-Recorders), the comparison revealed a small positive
297 temperature bias of $0.02\text{ }^{\circ}\text{C}$ and the depth (pressure) bias indicating depth overestimation.

298

299 **2.4 Climatology**

300 For IAP and other data product generators, horizontal interpolation (mapping) is
301 applied on a temperature anomaly field after removing a monthly climatology; thus, a pre-
302 defined climatology field with an annual cycle is mandatory (Fig. 2). The accuracy of the
303 climatology field is one of the key sources of uncertainty in reconstruction because the
304 error in climatology will propagate into the anomaly field, impact the spatial dynamical
305 consistency, and the accuracy of the reconstruction (Cheng and Zhu, 2015; Lyman and
306 Johnson, 2014; [Boyer et al., 2016](#)).

307 In IAPv4, the adjusted mapping procedure (see below) has been applied to reconstruct
308 the climatology field (Table 1). The merit of using IAP mapping for climatology is its
309 ability to better represent the spatial anisotropy of temperature variability (non-Gaussian
310 distribution). Unlike IAPv3, where the 1990–2005 reference period was used, IAPv4 uses
311 data between 2006 and 2020 to construct 12 monthly climatologies, taking advantage of
312 more reliable data combined with better and more homogeneous spatial and temporal
313 coverage in the last two decades (Table 1). Following the recommendation in Cheng and
314 Zhu, (2015), a relatively short period of 15-year is used because climatology constructed
315 with longer period of data will result in different baselines at different locations (i.e., the
316 baseline shifted to earlier years in the middle latitudes of the North Hemisphere and the
317 baseline shifted to more recent years in the Southern Hemisphere) and this inconsistency
318 will violate the spatial structure of the anomaly field (Cheng and Zhu, 2015). [Recent](#)

删除了: ive

删除了: Such a choice has been adopted by recent developments from other groups, such as Li et al., (2022)

322 developments from other groups, such as Li et al., (2022), include the choice of a short-
323 period climatology.

删除了: have adopted

324 IAPv4 used an 800 km influencing radii in climatology reconstruction, smaller than
325 the 20° for IAPv3, to more properly account for the rapid change of temperatures with
326 distance. There is a trade-off between data availability and the size of the influence radius.
327 Using radii smaller than 500 km does not ensure a global fractional coverage (defined as
328 the fraction of the total ocean area obtained by the mapping method) because of data
329 sparseness (Cheng, 2024). As our tests suggest, using 500~800 km results in very similar
330 reconstructions of climatology, therefore, 800 km is adopted.

331

332 2.5 Vertical interpolation

333 The vertical resolution of ocean temperature profiles changed dramatically over time
334 associated with instrument evolution and the increase of data storage capability. For
335 instance, the global mean vertical resolution at 500 m level changed from ~100 m in the
336 1960s to less than 10 m during the 2010s (Li et al., 2020). Vertical interpolation of the raw
337 profiles on standard levels is a critical process (Fig. 2): Cheng and Zhu (2014) indicated
338 that the use of linear or spline vertical interpolation methods can bias the temperature
339 reconstruction and OHC estimation (Barker and McDougall, 2020; Li et al., 2020; Li et al.,
340 2022). IAPv3 used the (Reiniger and Ross, 1968) (RR) method. Recently, Barker and
341 McDougall (2020) proposed a new approach using multiple Piecewise Cubic Hermite
342 Interpolating Polynomials (PCHIPs) to minimize the formation of unrealistic water masses
343 by the interpolation procedure.

删除了: The limitation of this method is that salinity data are needed for interpolation.

344 Because the largest difference between interpolation methods is found mostly for the
345 low-resolution profiles (e.g., old Nansen casts), in practice, extremely low vertical
346 resolution profiles had to be removed to reduce the uncertainty in interpolation. In IAPv4,
347 this procedure is optimized compared to IAPv3, and only parts of profiles with a sufficient
348 vertical resolution are used. The thresholds for the vertical resolution are set by 50 m in the
349 upper 200m, 200m between 200 m and 1000 m, 500 m between 1000 m and 2000 m, and
350 600m between 2000 m and 6000 m. As no interpolation method can adequately interpolate
351 temperature for the vertical resolution beyond these thresholds, interpolation is not
352 performed in such cases to avoid errors (these extreme low-resolution data are not used in
353 further processing). Under this limitation for IAPv4, we still apply the RR method for
354 temperature profiles.

358 Finally, IAPv4 extends the set of standard vertical levels with a total of 119 levels
359 from 1 m to 6500 m (79 levels within the upper 2000 m) compared to 41 levels in IAPv3
360 between 1 m and 2000 m (Table 1). The increase in vertical resolution is critical for
361 accurately representing the mixed layer, as investigated below.

362

363 2.6 Grid average and mapping

364 The anomaly profiles are obtained by subtracting the monthly mean climatology from
365 the vertically interpolated profiles. These anomalies are then averaged (arithmetic mean)
366 into a $1^\circ \times 1^\circ$ grid at each standard level ($1^\circ \times 1^\circ$ gridded average field) (Fig. 2). Due to the
367 general data sparsity, variable time windows (larger than one month) are used for monthly
368 reconstructions to ensure a truly global analysis (Supplementary Table 1). This process
369 takes advantage of the larger persistence of anomalies (generally smaller monthly and
370 inter-annual variability), in the deep ocean than in the upper ocean and thus is physically
371 grounded. Specifically, after 2005, data within a three-month window are merged to
372 provide a monthly reconstruction for each layer of the upper 1950 m. Before 2005, a time-
373 varying and depth-varying time window is used, and it is generally smaller in the upper
374 ocean and wider in the deeper ocean (Supplementary Table 1). Below 2000 m, a 5-year
375 (60-month) window is adopted. The use of a time window will reduce the monthly
376 variance compared to other datasets, which is likely too high compared with independent
377 Earth's Energy Imbalance data at the top of the atmosphere (Trenberth et al., 2016).

删除了: , especially in the deep ocean,

378 Mapping interpolates the gridded (e.g., box-averaged) observations horizontally into a
379 spatially complete map (Fig. 2) because not all $1^\circ \times 1^\circ$ boxes are filled with data. (Fig. 2).
380 IAPv4 adopted a similar mapping approach (Ensemble Optimal Interpolation with dynamic
381 ensemble: EnOI-DE) as in IAPv3 introduced in Cheng and Zhu (2016) and Cheng et al.,
382 (2017) but with the following modifications:

383 1) the largest influence radius has changed from 20° in the upper 700 m (25° at 700–
384 2000 m) in IAPv3 to 2,000 km in the upper 700 m (2,500 km at 700–6000 m) in IAPv4, to
385 account for the reduced distance between two longitudes from tropics to the polar regions.
386 This change mainly helps to improve the reconstruction in the high-latitude regions;

387 2) The three iterative runs are taken to effectively bring in different scales of
388 variability with influencing radius changing from 2,000 km (2,500 km at 700–6000 m) to
389 800 km and 300 km, respectively. based on the tests presented in Cheng and Zhu (2016)
390 and Cheng et al., (2017);

删除了： with real forcings

域代码已更改

域代码已更改

设置了格式：字体：加粗，倾斜

删除了：：

392 3) For each month, IAPv3 used 40 model simulations (historical runs) from the
393 Coupled Model Intercomparison Project phase 5 (CMIP5) to provide a flow-dependent
394 ensemble, which is then constrained by observations to provide optimized spatial
395 covariance. IAP mapping uses model-based covariance because we argue that spatial
396 covariance can never be satisfactorily parametrized by some simple basic functions (such
397 as Gaussian) given its complexity. With model-based, flow-dependent, and dynamically-
398 consistent covariance, the IAP mapping provides a more realistic reconstruction than other
399 approaches based on Gaussian-based parameterized covariance, as evaluated by many
400 studies (Cheng et al., 2017; Cheng et al., 2020; Dangendorf et al., 2021; Nerem et al.,
401 2018).

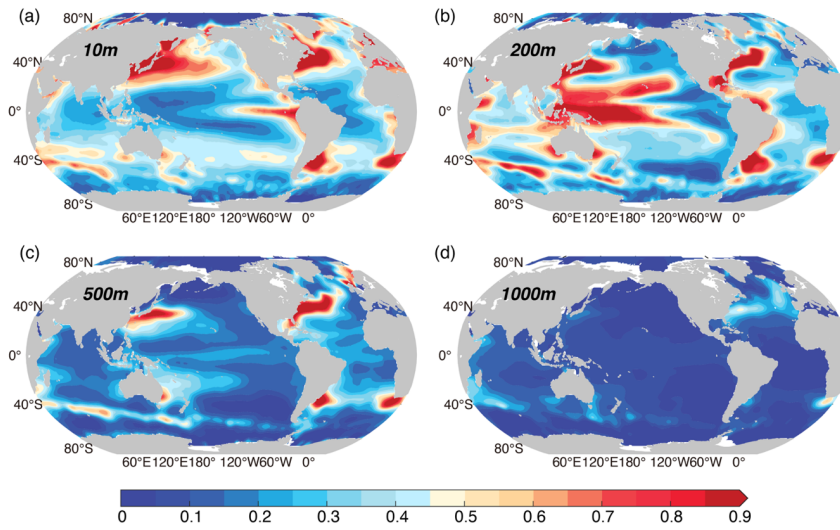
402 4) The observation error variance (\mathbf{R}), which represents the error of the observations,
403 is updated in IAPv4 as follows. \mathbf{R} consists of both the instrumental error (\mathbf{R}_e) due to
404 inaccuracy and the representativeness error (\mathbf{R}_r) due to the need to represent the spatial (at
405 1° by 1° and 1 m standard grid depths) and temporal (1 month) averages from a limited
406 numbered of observations (Cheng and Zhu, 2016):

$$407 \quad \mathbf{R} = \mathbf{R}_e + \mathbf{R}_r = \left(\sum_{i=1}^M \mathbf{E}i \right) / M + \sigma^2 / M,$$

408 where M observations exist for a given grid cell. $\mathbf{E}i$ is the instrument's precision for
409 each individual observation, assuming random error (the basic assumption is that after bias
410 correction, the systematic errors can be eliminated). \mathbf{R}_e in each grid cell is set to the mean
411 of the typical precision of the different instruments contributing data in the cell, which is
412 set according to IQuOD (International Quality-Controlled Ocean Database) specification
413 (Cowley et al., 2021). σ^2 represents the variance of the various temperature measurements
414 against the monthly mean value. The data from 2005 to 2022 are used to calculate σ^2 in
415 each grid because of greater data abundance and quality compared to earlier times.

416 As the representativeness error (\mathbf{R}_r) is expected to be flow-dependent (i.e., the error is
417 expected to be higher in areas with a large gradient of the flow speed and regions of higher
418 variability), more observations are required to represent the mean value. Figure 4 shows a
419 larger variance (σ^2) in the boundary-current regions and near the Antarctic Circumpolar
420 Current (ACC) in the upper ocean (e.g., 10 m, 200 m, 500 m). At 200 m, it shows a larger
421 σ^2 in the Western Pacific Ocean, corresponding to the large thermocline variations at this
422 layer. Below 1000 m, larger σ^2 along the ACC frontal regions and in the North Atlantic
423 Ocean occur because of a stronger mixing and convection in these regions.

426 The uncertainty in the derived gridded reconstruction is also based on the EnOI
 427 framework formulated by Cheng and Zhu, (2016). The uncertainty accounts for
 428 instrumental, sampling and mapping errors. Other error sources, including the choice of
 429 climatology, vertical interpolation, bias corrections, and QC, are not considered in this
 430 uncertainty estimate. Therefore, a more thorough uncertainty quantification method is
 431 needed, and this is under development in a separate study.



432

433

434

435

Figure 4: Variance (σ^2) of ocean temperature at several representative layers. (a) 10 m, (b) 200 m, (c) 500 m and (d) 1000 m. The unit is $^{\circ}\text{C}^2$.

删除了: Variance

删除了: degree Celsius

设置了格式: 上标

436

Table 1. General information on IAPv4 and IAPv3 data products.

	IAPv3	IAPv4
Horizontal resolution	Global ($1^{\circ} \times 1^{\circ}$)	Global ($1^{\circ} \times 1^{\circ}$)
Vertical levels	41 levels from 1 m to 2000 m (1, 5, 10, 20, 30, 40, 50, 60, 70, 80, 90, 100, 120, 140, 160, 180, 200, 250, 300, 350, 400, 450, 500, 550, 600, 650, 700, 750, 800, 850, 900, 1000, 1100, 1200, 1300, 1400, 1500, 1600, 1700, 1800, 2000)	119 levels from 1 m to 6000 m (1, 5, 10, 15, 20, 25, 30, 35, 40, 45, 50, 55, 60, 65, 70, 75, 80, 85, 90, 95, 100, 110, 120, 130, 140, 150, 160, 170, 180, 190, 200, 220, 240, 260, 280, 300, 320, 340, 360, 380, 400, 425, 450, 475, 500, 525, 550, 575, 600, 625, 650, 675, 700, 750, 800, 850, 900, 950, 1000, 1050, 1100, 1150, 1200,

		1250, 1300, 1350, 1400, 1450, 1500, 1550, 1600, 1650, 1700, 1750, 1800, 1850, 1900, 1950, 2000, 2100, 2200, 2300, 2400, 2500, 2600, 2700, 2800, 2900, 3000, 3100, 3200, 3300, 3400, 3500, 3600, 3700, 3800, 3900, 4000, 4100, 4200, 4300, 4400, 4500, 4600, 4700, 4800, 4900, 5000, 5100, 5200, 5300, 5400, 5500, 5600, 5700, 5800, 5900, 6000)
Time period and resolution	1940–2022 (reliable data after 1955), monthly	1940–present (reliable data after 1955), monthly
Quality-control	WOD (Garcia et al., 2018)	CODC-QC (Tan et al., 2023)
Vertical interpolation	RR (Reiniger and Ross, 1968) interpolation	RR (Reiniger and Ross, 1968) interpolation
Climatology	IAP climatology: simple gridded average and then spatial interpolation with distance-weighted average	Improved IAP reconstruction with EnOI approach
XBT bias correction	CH14 (updated in 2018)	CH14 (revised and updated in 2023)
MBT bias correction	IK09 (Ishii and Kimoto, 2009)	GC20 (Gouretski and Cheng, 2020)
APB bias correction	None	GCR24 (Gouretski et al., 2024)
Bottle bias correction	None	GCT22 (Gouretski et al., 2022)
Mapping	EnOI-DE with influencing radius of 20, 8, 3 degrees, iteratively.	EnOI-DE with influencing radius of 2000, 800, 300 km, iteratively. Representative error updated with 2005–2022 observations. <u>The radius of influence does not cross the land.</u>
Uncertainty	Given by EnOI framework accounting for instrumental error and horizontal sampling/mapping error	Given by EnOI framework accounting for instrumental error and horizontal sampling/mapping error
DOI	/	http://dx.doi.org/10.12157/IOCAS.20240117.002 for temperature data (Cheng et al., 2024a) and http://dx.doi.org/10.12157/IOCAS.20240117.001 for ocean heat content data (Cheng et al., 2024b).

删除了: YES

441 2.7 OHC calculation and volume correction

442 Based on the gridded temperature reconstruction (Table 1), OHC in each grid is
443 calculated as $OHC(x, y, z) = c_p \iiint_{V(x,y,z)} \rho T dV(x, y, z)$. following TEOS-10 standards,
444 where c_p is a constant of $\sim 3991.9 \text{ J (kg K)}^{-1}$ according to the new TEOS-10 standard
445 formulation as conservative temperature and absolute salinity are used, ρ is potential
446 density in kg m^{-3} , and T is conservative temperature measured in degrees Celsius (here it
447 is anomaly relative to the 2006–2020 baseline) (Cheng et al., 2022a).

448 As OHC is an integrated metric over a specific ocean volume, properly identifying
449 ocean volume is critical, especially in shallow waters. Previous studies found a 10–20 %
450 difference in the OHC trend in recent decades between different land-ocean masks (von
451 Schuckmann and Le Traon, 2011; [Meysignac et al., 2019](#); [Savita et al., 2022](#)).
452 Specifically, in marginal sea areas with complex topography, $1^\circ \times 1^\circ \times \Delta z$ grid boxes
453 (where Δz is the depth range of the grid box) near coasts and islands typically cover both
454 ocean and land areas but are assigned to represent land or ocean only. Thus, the gridded
455 ocean temperature datasets are subjected to errors from inaccurate land-sea attribution.
456 Here, we offer a volume correction (VC) for these grid boxes to improve the OHC
457 estimate, as follows.

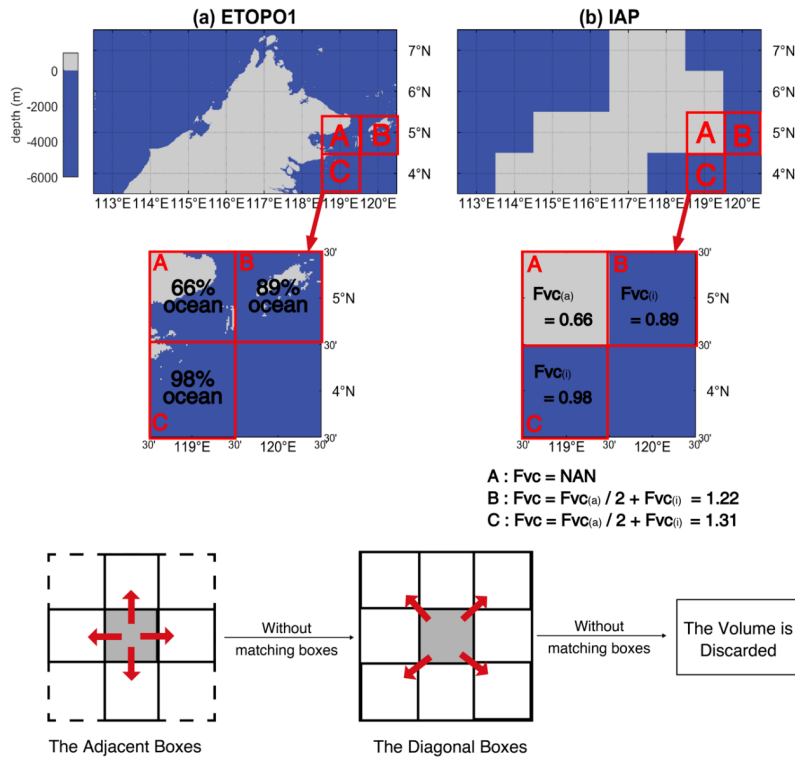
458 For each $1^\circ \times 1^\circ \times \Delta z$ grid box, we introduce a VC factor (denoted as F_{VC}) to correct
459 the OHC values: $OHC_{VC}(x, y, z) = OHC(x, y, z) \times F_{VC}(x, y, z)$. First, we assume the
460 seawater volume distribution in 1 arc-minute topographic data of ETOPO1 as “truth”. No
461 correction is needed if a box is assigned to ocean according to ETOPO1 data, thus, $F_{VC}=1$.
462 If a fraction of a $1^\circ \times 1^\circ \times \Delta z$ grid box is land according to ETOPO1 and IAP data includes
463 T/OHC values, the F_{VC} is represented by the fraction of the ocean volume in this box
464 (illustrated in Fig. 5), and the volume for OHC calculations can be corrected with $F_{VC}(i)$. In
465 a grid box, if there is no IAP data (i.e., it is land according to the IAP mask), but this box
466 contains some ocean volume according to ETOPO1 data, we define $F_{VC}(a)$ again as the
467 fraction of the ocean volume in this box, and then this $F_{VC}(a)$ is added to the adjacent grid
468 boxes where there are values in IAP data. If all the adjacent grid boxes contain no data, the
469 volume is equally redistributed to the diagonal boxes (Fig. 5). The volume is discarded if
470 there is no data in all adjacent and diagonal boxes.

471 With this approach, the VC factor in each grid box is a sum of two components: a
472 local adjustment $F_{VC}(i)$ and a redistribution from the adjacent grids:

473
$$F_{VC}(a) = F_{VC}(i) + F_{VC}(a),$$

474 To avoid misidentification of sea ice, we performed VC only on the global grid points
475 within 60 °S to 60 °N. Eventually, we obtained a three-dimensional FVC that fits the IAP
476 grids (119 × 360 × 180; depth coverage to 6000 m) and used it to compute OHC. The VC
477 applied to ~15% of all the $1^\circ \times 1^\circ \times \Delta z$ grid boxes of IAPv4 ocean grid boxes (with $F_{VC} \neq$
478 1) for the entire 0-6000 m ocean and ~10% grid boxes of the upper 2000 m. Since the open
479 ocean accounts for the vast majority of the global ocean volume, the influence of the VC
480 method on the global OHC trend is small. For example, the upper 2000 m OHC trend with
481 VC is ~0.15% (~0.45%) smaller than without VC from 1958-2023 (2005-2023) for IAPv4.
482 However, it can significantly affect regional OHC estimates, especially in regions with
483 complex topography. For example, the Maritime Continent region's 0-2000 m OHC trend
484 is reduced by 6.9% (4.2%) after applying VC from 1958-2023 (2005-2023) (Jin et al.,
485 2024).

设置了格式: 字体: (中文) 宋体, 12 磅, 字体颜色:
文字 1



486

487 **Figure 5:** An example explaining the Volume Correction algorithm. (a) Bathymetry

488 derived from ETOPO1. (b) Bathymetry in IAPv4 analysis.

489

490 2.8 Independent datasets for comparison and evaluation

491 Four Sea Surface Temperature (SST) datasets are used to evaluate the upper-most
 492 layer (1 m) of IAPv4, including Extended Reconstructed SST version 5 (ERSST5) (Huang
 493 et al., 2017); Japan Meteorological Agency Centennial Observation-Based Estimates of
 494 SSTs version 1 (COBE1) (Ishii et al., 2005), and its version 2: COBE2 (Hirahara et al.,
 495 2014); Hadley Centre Sea Ice and Sea Surface Temperature dataset (HadISST) (Rayner et
 496 al., 2003). The anomalies relative to a 2006-2020 average were computed by removing the
 497 monthly climatology. Measurements of SST are made *in situ* by means of thermometers or
 498 retrieved remotely from infrared and passive microwave radiometers on satellites
 499 (Kennedy, 2014; O'Carroll et al., 2019). Satellite SST observations began in the early

500 1980s. *In situ* SST observations go back to the 19th century and involve many different
501 measurement methods, including wooden and later insulated metal buckets to collect water
502 samples, engine room inlet measurements, and sensors on moored and drifting buoys
503 (Kennedy, 2014). The subsurface temperatures are collected as “profiles” which contain
504 multiple measurements at discrete vertical levels. Because of the differences in observation
505 systems, SSTs are fundamentally different in their temporal and spatial coverage and
506 temporal extent compared to subsurface observations on which OHC estimates rely. SST
507 measurements also have different uncertainty sources and error structures; thus, the two
508 systems are typically treated as independent data sources and have been used for cross-
509 validation (Gouretski et al., 2012).

510 An independent *in situ* observation dataset in the Labrador Sea is used to evaluate
511 IAPv4. This dataset, provided by the Bedford Institute of Oceanography (BIO)
512 (Yashayaev, 2007; Yashayaev and Loder, 2017), includes independently validated and
513 bias-corrected data from multi-section hydrological surveys (i.e., AR7W) in the Labrador
514 Sea, spanning from 1896 to 2020 (this study used 1960-2020 data). These data have not
515 been incorporated into the WOD.

删除了： collected and

删除了： in situ

删除了： is

删除了： ing the

删除了： , thus we used these data to evaluate the IAPv4.

516 The capability of the new product to close the sea level budget and the Earth’s energy
517 budget also provides tools for validation. A superior dataset should be capable of closing
518 the sea level and the Earth’s energy budgets. The total sea level change has been monitored
519 via satellite altimetry since 1993 (from the University of Colorado
520 <https://sealevel.colorado.edu/>). The ocean mass change is derived from JPL RL06.1Mv3
521 Mascon Solution GRACE and GRACE-FO data since 2002 (Watkins et al., 2015). For
522 long-term total sea level change since the 1950s, we use a tide-gauge-based reconstruction
523 (Frederikse et al., 2020). During the same period, the estimates of the Greenland ice sheet,
524 Antarctic ice sheet, land water storage, and glacier ice melt contributions from Frederikse
525 et al., (2020) are used to derive ocean mass change. To derive steric sea level, IAP salinity
526 data is used (Cheng et al. 2020). The temperature and salinity data are converted to steric
527 sea level based on the Thermodynamic Equation Of Seawater – 2010 (TEOS-10) standard
528 (McDougall and Barker, 2011).

529 For the energy budget, the ice, land, and atmosphere heat content changes are from
530 (von Schuckmann et al., 2023) from 1960 to the present. Because of the less reliable data
531 before the 1990s for land, sea ice and ice sheets, the other set of land–atmosphere–ice data
532 from 2005–19 is used as in Trenberth, (2022) to investigate the recent changes. The net

538 radiation change at the top of the atmosphere is based on [Clouds and Earth's Radiant](#)
539 [Energy Systems \(CERES\) Energy Balanced and Filled \(EBAF\)](#) data from Loeb et al.,
540 (2021) and Loeb et al., (2018) and Deep-C data from the University of Reading (Liu and
541 Allan, 2022; Liu et al., 2017).

删除了: CERES EBAF

542 Several gridded ocean T/OHC gridded products are used here for inter-comparison,
543 including the IAPv3 (Cheng et al., 2017), the EN4 ocean objective analysis product from
544 the UK Met Office Hadley Centre (Good et al., 2013); the ocean objective analysis product
545 (Ishii et al., 2017) (termed “ISH” hereafter) from JMA, [an Argo-only gridded product from](#)
546 [SCRIPPS \(Roemmich and Gilson, 2009\) \(termed “RG” hereafter\), and an OHC product](#)
547 [based on random forest regressions \(termed “RFROM” hereafter\) using in situ training](#)
548 [data from Argo and other sources on a 7-day × 1/4° × 1/4° grid with latitude, longitude,](#)
549 [time, SSH, and SST as predictors \(Lyman and Johnson, 2023\). Several datasets available](#)
550 [in IPCC-AR6 \(Gulev et al., 2023\) are used for comparison, including: the PMEL product](#)
551 [from Lyman and Johnson, \(2014\); Machine learning based reconstruction of OHC by](#)
552 [Bagnell and DeVries, \(2021\); BOA product based on refined Barnes successive corrections](#)
553 [by the China Argo Real-time Data Center \(Li et al., 2017\); International Pacific Research](#)
554 [Center \(IPRC\) \(2005-2020\), von Schuckmann and Le Traon 2011 \(KvS11\); Green function](#)
555 [based OHC estimate derived from SST \(Zanna et al., 2019\).](#)

删除了: and

556

557 **2.9 Trend calculation and uncertainty estimates**

558 The trends in this study have been estimated by a LOWESS approach (Cheng et al.,
559 2022b), i.e., we apply a locally weighted scatterplot smoothing (LOWESS) to the time
560 series (25-year window, equal to an effective 15-years smoothing), and then the OHC
561 difference between the first and the end year is used to calculate the trend. This approach
562 provides an effective method to quantify the local trend by minimizing the impact of year-
563 to-year variability and start/end points.

564 Throughout this paper, the 90 % confidence interval is shown. The uncertainty of
565 trend also follows the approach in Cheng et al., (2022a) based on a Monte Carlo
566 simulation. First, a surrogate OHC series is formed by simulating a new residual series
567 (after removing the LOWESS smoothed time series) based on the AR(1) process and
568 adding it to the LOWESS line. Then a LOWESS trendline is estimated for each surrogate.
569 This process is repeated 1000 times, and 1000 trendlines are available. The 90 %
570 confidence interval for the trendline is calculated based on ± 1.65 times the standard

573 deviation of all 1000 trendlines of the surrogates. Secondly, the uncertainty in the rate of
574 the OHC is estimated by the 1000 LOWESS trendlines: 1) calculating the rate based on the
575 difference between the first and last annual mean value of the LOWESS trendline in a
576 specific period; 2) calculating ± 1.65 times the standard deviation of the 1000 rate values.

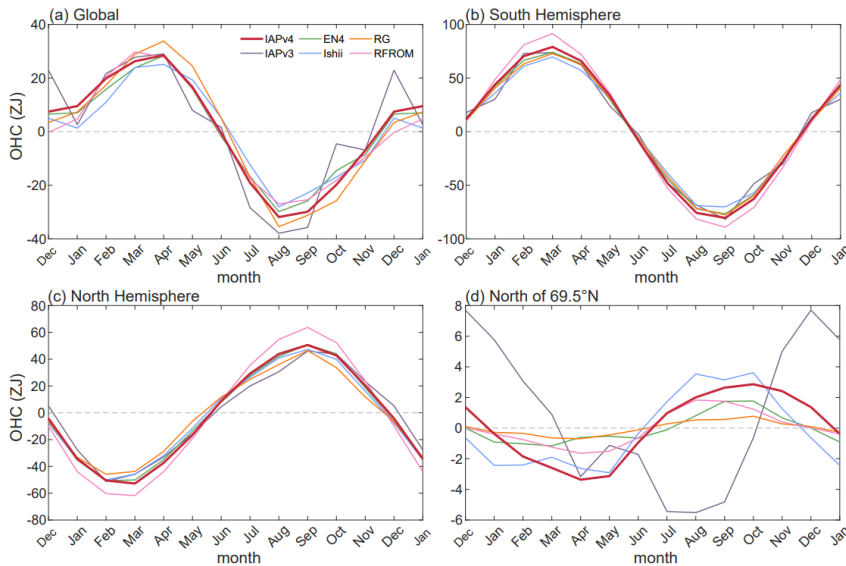
577

578 **3. Results**

579 **3.1 Climatological annual cycle**

580 The annual cycle of the OHC above 2000 m of IAPv4 is compared with IAPv3, ISH,
581 EN4, RG and RFROM (Fig. 6 and Fig. 7) for 2006–2020. There is a consistent annual
582 cycle among different datasets for the global and hemispheric oceans. Globally, the ocean
583 releases heat from boreal spring to autumn and accumulates heat from boreal autumn to
584 spring, which is dominated by the southern hemisphere due to its larger ocean [surface](#) area
585 (Fig. 6). The two hemispheres show opposite annual variations in OHC, associated with
586 the annual change of solar radiation and different distribution of land and sea. For the
587 global OHC above 2000 m, IAPv4 shows a positive peak in April and a dip in August,
588 with the magnitude of OHC variation of 60.4 ZJ for IAPv4 (66.9 ZJ for IAPv3), consistent
589 with other datasets: 53.2 ZJ for ISH, 58.1 ZJ for EN4, 69.2 ZJ for RG [and 56.6 ZJ for](#)
590 [RFROM](#) (where 1 ZJ = 10^{21} J).

591 There are some unphysical variations in the OHC annual variations for IAPv3 (blue
592 lines). For example, the global OHC shows large spikes in January and December, and a
593 big shift from September to October, by contrast, the other three data products show much
594 smoother changes (Fig. 6a). The IAPv3 Arctic OHC (north of 69.5 °N) shows different
595 phase change compared with the other datasets together with a big shift from September to
596 December, and the magnitude of variability is much larger in IAPv3 than other datasets
597 (Fig. 6d). The improvement in IAPv4 is mainly because of the methodology
598 improvements: IAPv3 used 1990–2005 data to construct climatology which suffered from
599 errors related to sparse data coverage, use of “degree distance” instead of “km distance”,
600 and other error sources. Therefore, the IAPv4 analysis presents a physically tenable OHC
601 seasonal variation.



602
603
604 **Figure 6: Annual cycle of OHC of upper 2000 m for (a) the global oceans, (b) the**
605 **Southern Hemisphere, (c) the Northern Hemisphere and (d) the oceans north of**
606 **69.5°N. Five different data products are presented, including IAPv4 (red), IAPv3 (black),**
607 **ISH (purple), EN4 (green), RG (orange), and RFROM (pink).**

608
609 IAPv4 OHC data shows significant improvements in the Arctic region, reflected in
610 both the spatial distribution and seasonal variation of OHC. In IAPv3, the maximum upper
611 2000 m OHC occurs in December, and the minimum OHC occurs in August. However, for
612 IAPv4, the maximum amounts to 2.9 ZJ in October and decreases to a minimum of -3.4 ZJ
613 in April. The spread of the OHC annual cycle in the Arctic region across different datasets
614 is reduced from 5.2 ZJ to 2.5 ZJ, indicating a smaller uncertainty. The spatial OHC
615 anomaly distribution in the Arctic region of the IAPv4 is more spatially homogeneous than
616 IAPv3, and IAPv3 appears as rays emerging from the pole which are not physical (Fig. 7).
617 IAPv4 displays a consistent seasonal variation north of 69.5 °N mainly because of the
618 changes of the influencing radius from “degrees” to “kilometers”.

删除了: blue

删除了: and

设置了格式: 字体: (默认) Times New Roman, 12 磅, 字体颜色: 文字 1

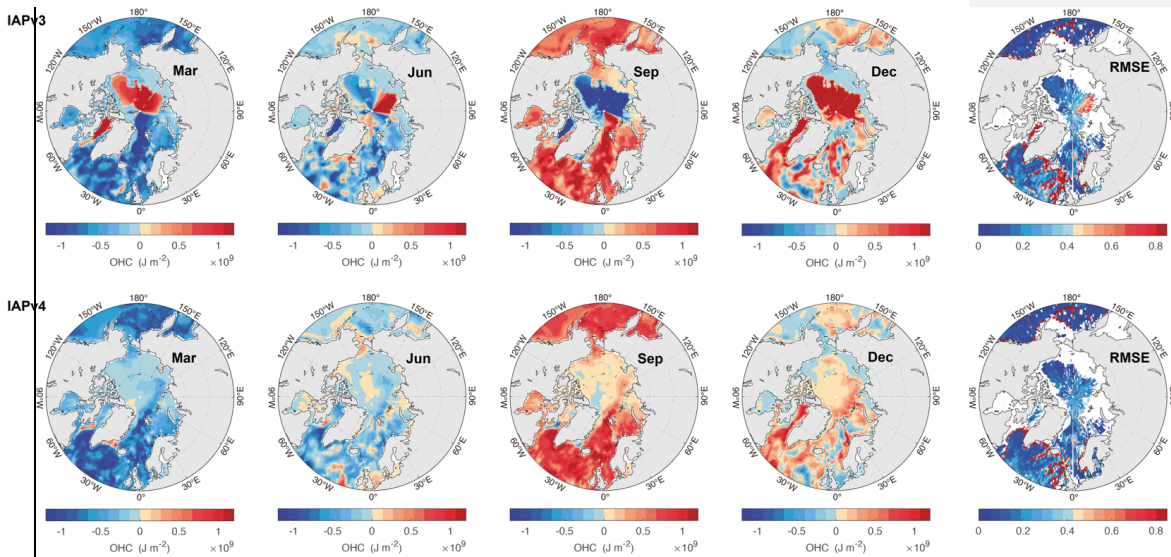
删除了: change

删除了: during December

删除了: ,h

删除了: which

删除了: seems not physical



627 **Figure 7: Seasonal distribution of monthly mean upper 2000 m OHC anomalies**
 628 **and root mean square error (RMSE) of OHC 0-2000 m between gridded data and in**
 629 **situ observations. For OHC anomalies, four months are shown: March, June,**
 630 **September, and December. The OHC anomalies are relative to the 2006 – 2020**
 631 **annual mean. The upper and lower panels are for IAPv3 and IAPv4 products,**
 632 **respectively. The panels in the last column are for annual RMSE for IAPv3 (upper) and**
 633 **IAPv4 (lower), respectively.**

删除了： OHC anomalies in the upper 2000 m in March, June, September, and December

删除了： top

删除了： a

删除了： , respectively

635 3.2 Mixed layer depth

636 Mixed layer depth (MLD) provides a crucial parameter of upper ocean dynamics
 637 relevant for upper-deeper ocean and air-sea interactions. Spatial distributions of the MLD
 638 in March and August are shown in Fig. 8 for IAPv4, based on criteria of $\Delta T = 0.2 \text{ }^\circ\text{C}$
 639 temperature for the 10 m depth temperature. As expected, the seasonal variations of the
 640 MLD are generally opposite in the northern and southern hemispheres. The MLD shows a
 641 much stronger seasonal variation in the subtropics and midlatitudes (for example, 20°~70°
 642 in both hemispheres) than in other regions (including the tropics, for example,
 643 20°S~20°N), which is manifested as shallower MLD (~20 m) in summer due to strong
 644 surface heating that increases stratification, and deeper MLD in winter (>70 m) because of
 645 surface cooling and increased surface wind creating stronger mixing.

删除了： January

删除了： July

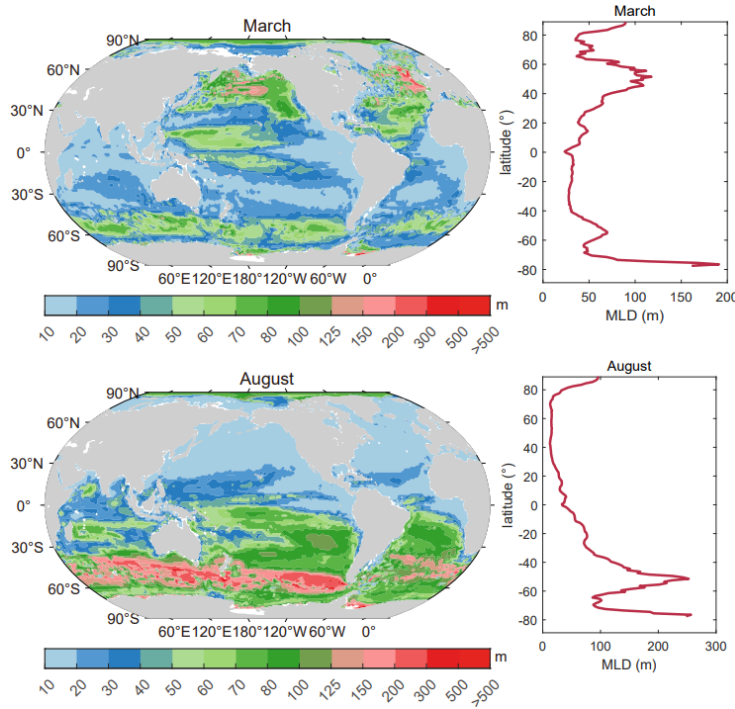
653 In the north hemisphere, the maximum MLD occurs during the wintertime in the
 654 subpolar North Atlantic deep water formation regions (40 °N ~ 65 °N), with values over
 655 500 m in the Iceland Basin. In comparison, in the midlatitudes, the maximum of MLD is
 656 generally less than 125 m in the wintertime. The MLD minimum in the north hemisphere is
 657 in the summertime, and the values are mostly within 20 m depth. In the Southern
 658 Hemisphere, the MLD maximum values (deeper than 300 m) occur between 45 °S and
 659 60 °S of the Southern Ocean (north of the Antarctic Circumpolar Current) in the boreal
 660 summer where the year-round intense westerly winds are located. The minimum MLD in
 661 this region in the boreal winter is less than 70 m. The seasonal variation of the MLD is
 662 well established by previous studies (Chu and Fan, 2023; de Boyer Montégut et al., 2004;
 663 Holte et al., 2017), and this evaluation confirms that IAPv4 temperature data is capable of
 664 reasonably representing the MLD. However, as pointed out by de Boyer Montégut (2004),
 665 the MLD estimated from the average temperature profiles might lead to an underestimation
 666 of MLD by ~25% compared to the MLD computed from individual profiles based on the
 667 same 0.2 °C criterion method. This potential issue needs further investigation.

删除了: Norway

删除了: Sea

删除了: .

删除了: may bias our calculation, which



668

673 **Figure 8: Spatial pattern of the climatological mean MLD (left panels) and zonal**
674 **mean MLD (right panels) in March (top) and August (bottom) estimated from the**
675 **IAPv4.** Here, the MLD is calculated using the temperature difference criterion of $\Delta T =$
676 $0.2\text{ }^{\circ}\text{C}$ between the surface and 10-meter depth.
677

删除了: January

删除了: July

删除了: 0

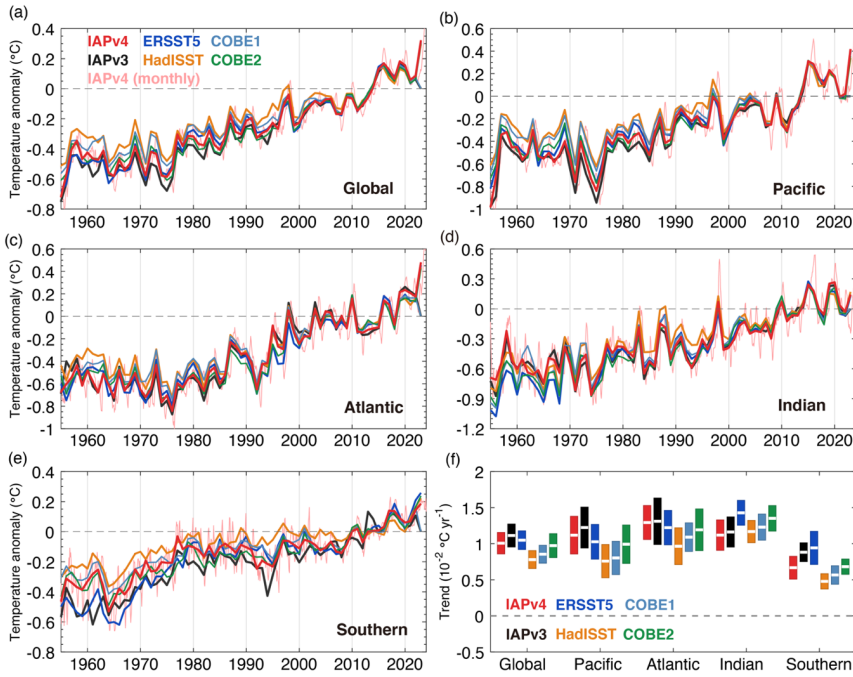
678 3.3 Sea surface temperature

679 IAPv4 and IAPv3 temperature time series at 1 m depth (Fig. 9) are compared with
680 four independent SST data products (ERSST5, HadISST, COBE1, and COBE2). All data
681 products including IAPv4 show robust sea surface warming in the global ocean and four
682 main basins since 1955 (Fig. 9). Since the HadISST and COBE2 data did not include the
683 year 2023, we compare the long-term SST trend during 1955–2022 using these products
684 (Fig. 9f). The global-mean IAPv4 SST rate between 1955 and 2022 is $1.01 \pm 0.15\text{ }^{\circ}\text{C}$
685 century^{-1} (90 % CI), which is within the range of the SST products (ranging from 0.78 to
686 $1.05\text{ }^{\circ}\text{C century}^{-1}$). The 1955–2022 trend of IAPv4 SST is slightly weaker than IAPv3 for
687 the global ocean ($1.11 \pm 0.16\text{ }^{\circ}\text{C century}^{-1}$) and all the ocean basins. The largest difference
688 between IAPv4 and other SST products comes mainly from the Pacific and the Southern
689 Ocean before 1980, associated with sparser in situ observations for both SST and
690 subsurface temperature data.

删除了: , and IAPv4 shows a quantitatively consistent warming rate...

691 The spatial distribution of long-term SST trends over the 1955–2022 period provides
692 insights into the data consistencies and differences. First, IAPv4 shows a pattern of SST
693 consistent with other datasets (Fig. 10). More rapid warming is found in the poleward
694 western boundary currents regions, such as the East Australian Current and the Gulf
695 Stream. The warmer ocean in the upwelling areas, such as the Tropical Eastern Pacific and
696 Gulf of Guinea, are identified by all data products. The surface warming in the South
697 Indian for IAPv4 data is weaker than for IAPv3, ERSST5, and COBE2 but is more
698 consistent with HadISST and COBE1. The surface cooling to the south of $60\text{ }^{\circ}\text{S}$ can also
699 be found in all the datasets but with some discrepancies in magnitude and locations related
700 to data sparsity. The tropical Pacific SST trends are mostly insignificant in the eastern and
701 south-eastern Pacific Ocean because of the strong inter-annual and decadal fluctuations
702 (Figure not shown).

删除了: in



709

710

711

712

713

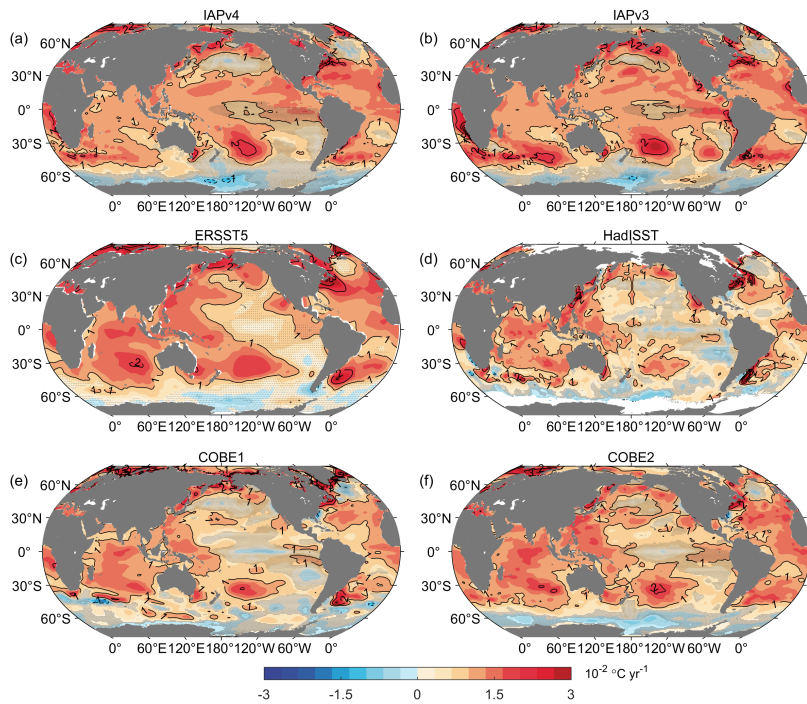
714

715

716

717

Figure 9: Global and basin time series of SST change for IAPv4, compared with ERSST/HadISST/COBE1/COBE2 and IAPv3 from 1955 to present. (a) Global, (b) Pacific, (c) Atlantic, (d) Indian and (e) Southern oceans (South of 30 °S) (units: °C). (f) shows the warming rate from 1955 to 2022. The pink thin line is the monthly time series of IAPv4 SST and other time series are annual time series of different datasets. The vertical scales are different for different panels. All anomaly time series are relative to a 2006–2020 baseline.



718

719 **Figure 10: Spatial maps of the SST long-term trends during the 1955–2022 period.** (a)
 720 IAPv4, (b) IAPv3, (c) ERSST5, (d) HadISST, (e) COBE1 and (f) COBE2 (units: $10^{-2} \text{ }^{\circ}\text{C}$
 721 yr^{-1}). The contour line interval is $0.5 \times 10^{-2} \text{ }^{\circ}\text{C yr}^{-1}$. The stippling indicates the regions with
 722 signals that are not statistically significant (90 % CI).

723

724 3.4 Global OHC time series

725 Global OHC time series for 0–700 m, 700–2000 m, 0–2000 m, and 2000–6000 m
 726 layers of IAPv4 (Fig. 11) for 1955–2023 versus IAPv3 show a robust ocean warming, with
 727 a linear warming rate of $4.4 \pm 0.2 \text{ ZJ yr}^{-1}$ (0–700 m), $2.0 \pm 0.1 \text{ ZJ yr}^{-1}$ (700–2000 m), and
 728 $6.4 \pm 0.3 \text{ ZJ yr}^{-1}$ (0–2000 m). The long-term warming revealed by IAPv4 is greater than
 729 IAPv3 ($4.1 \pm 0.2 \text{ ZJ yr}^{-1}$ for 0–700 m, $1.9 \pm 0.1 \text{ ZJ yr}^{-1}$ for 700–2000 m and 6.0 ± 0.3
 730 ZJ yr^{-1} for 0–2000 m). Before ~1980, bottle bias correction reduces the time-varying
 731 systematic warm bias in Nansen bottle data and leads to a stronger warming rate from
 732 1955–1990. The updated MBT and XBT corrections are mainly responsible for the

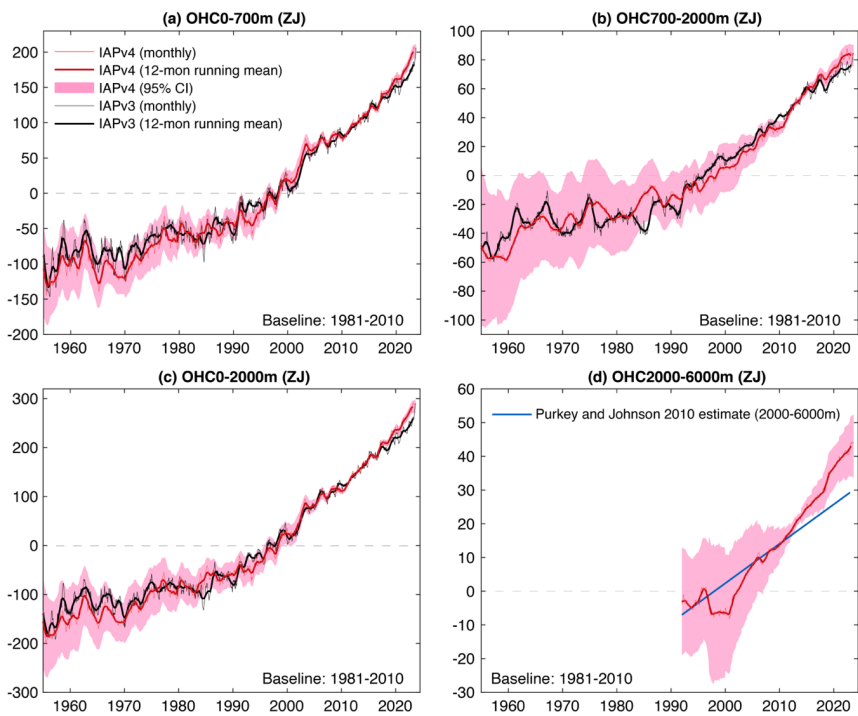
删除了: month-to-month

733 difference between 1980 and 2000 (Cheng et al., 2014; Gouretski and Cheng, 2020). Data
734 QC impacts the intra-seasonal and inter-annual variation of the OHC time series (Tan et
735 al., 2023). Also, because of the application of Bottle/XBT/MBT corrections, IAPv4 shows
736 a stronger upper 2000 m ocean warming trend than most of the other available products
737 assessed in Fig. 12.

738 From 2005–2023, the new IAPv4 product shows stronger warming than IAPv3. The
739 mean upper 2000 m warming rate is 10.7 ± 1.0 ZJ yr⁻¹ for IAPv4 and 9.6 ± 1.1 ZJ yr⁻¹ for
740 IAPv3 (Fig. 11), mainly because of the replacement of the WOD-QC system by the new
741 CODC-QC system in IAPv4. Tan et al., (2023) indicated that the WOD-QC system had
742 removed more extreme higher temperature values in the regions of warm eddies and
743 marine heat waves than CODC-QC. The IAPv3 700–2000 m OHC shows a much bigger
744 drop in 2018 than IAPv4 (Fig. 11b), while the IAPv4 indicates an approximately linear
745 700–2000 m warming since 2005, resulting in stronger 700–2000 m warming in IAPv4
746 (3.6 ± 0.5 ZJ yr⁻¹) than in IAPv3 (2.9 ± 0.5 ZJ yr⁻¹). Compared with other available
747 products shown in Fig. 12, IAPv4 shows a similar OHC 0–2000 m trend to RFROM from
748 2005–2023, but with stronger warming trends than the two Argo-based products (BOA and
749 SCRIPPS). From 1993–2023, IAPv4 showed a stronger OHC 0–2000 m trend than NCEI,
750 Ishii, OPEN, and Zanna data and a slightly weaker trend than PMEL and RFROM (Fig.
751 12).

752 Since the 1990s, the World Ocean Circulation Experiment (WOCE) provided a global
753 network of abyssal ocean observations, sustained by repeated hydrological lines and a
754 deep-Argo program (Katsumata et al., 2022; Roemmich et al., 2019; Sloyan et al., 2019).
755 These high-quality data provide an opportunity to estimate deep OHC changes below 2000
756 m in this study. IAPv4 provides a new OHC estimate below 2000 m by collecting 5 years
757 of data centered on each month. The result (Fig. 11d) indicates a robust abyssal (2000–
758 6000 m) ocean warming trend since ~1993 of 2.0 ± 0.3 ZJ yr⁻¹. This is higher (within the
759 uncertainty range) than the previous estimate of 1.17 ± 0.5 ZJ yr⁻¹ in Purkey and Johnson
760 (2010) but consistent with the recent assessment showing the acceleration of deep ocean
761 warming in the Southwest Pacific Ocean (Johnson et al., 2019).

762



764

765 **Figure 11: Global OHC time series for 0–700 m (a), 700–2000 m (b), 0–2000 m (c) and**

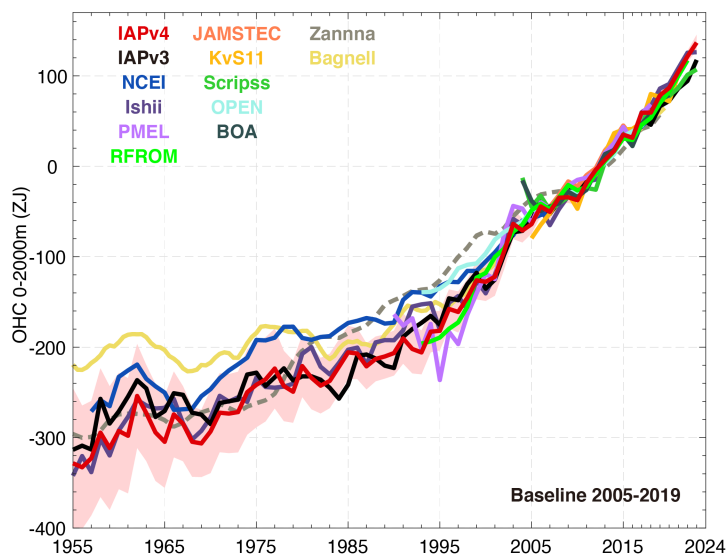
766 **2000–6000 m (d).** All-time series are relative to a 1981–2010 baseline. The shading

767 indicates the 90 % confidence interval. The vertical scales are different for different panels.

768

The unit is ZJ.

769



770
771 **Figure 12: A comparison of annual mean OHC 0-2000 m time series from different**
772 **data products. Solid and dashed lines represent direct and indirect estimates, respectively,**
773 **and shading indicates the IAPv4 90% confidence interval (pink shading). OHC anomalies**
774 **are relative to a 2005–2019 baseline. The plot is updated from Cheng et al. (2022a).**

775
776 Another feature of IAPv4 is the suppression of month-to-month noise compared to
777 many available data products. Trenberth et al. (2016) noted that the month-to-month
778 variation (quantified by the standard deviation of the monthly $dOHC/dt$ time series) in all
779 *in situ*-based OHC records is much larger than implied by the CERES records, suggesting
780 that the OHC variation on this time scale is most likely spurious. Therefore, the magnitude
781 of the month-to-month variation in the OHC record can be used as a benchmark of the data
782 quality. The standard deviation of the CERES record is 0.67 Wm^{-2} from 2005 to 2023
783 (Loeb et al., 2018). While IAPv4, IAPv3, ISH, EN4, BOA, NCEI, and SIO data show a
784 standard deviation of $dOHC/dt$ time series of 3.52, 3.52, 7.49, 8.79, 10.05, 11.29, 10.00
785 Wm^{-2} , respectively **for the upper 2000 m** (Table 2). Note that differentiation to get the rate
786 of change amplifies noise, and applying a 12-month running smoother significantly knocks
787 down the noise so that the IAPv4 standard deviation becomes 0.75 Wm^{-2} , the smallest
788 among the datasets investigated in this study (Table 2) and is the most physically plausible
789 time series from this noise-level perspective. **In addition, Lyman and Johnson's (2013) data**

771 设置了格式: 字体: 非加粗

772 设置了格式: 字体: 非加粗

773 设置了格式: 字体: 非加粗

774 设置了格式: 字体: 非加粗, 字体颜色: 自动设置

784 删除了:

suggest a yearly variance ratio of 1.3 between annual RFROM and CERES data from 2008 to 2021. Using the yearly mean OHCT indicates a ratio of 1.4 at the same period between IAPv4 and CERES, which is similar to that of RFROM.

Table 2. Characteristics of Month-to-month variation of OHCT compared with CERES. Comparisons of different ocean gridded products: the monthly standard deviation (std dev) of the monthly rates of change of OHC (W_m^{-2}); the corresponding standard deviation of the 12-month running mean (13-points are used, with start-point and endpoint weighted by 0.5), and the linear trend with 90% confidence limits (W_m^{-2}) (global surface area). The values are for 2005–2022. The OHC trend for CERES is calculated as the mean of net TOA radiation flux within 2005–2022 multiplied by 0.9, assuming 90% of the EEL stored in the ocean.

Source	Std dev	Std dev (12 month)	OHC Trend (2005–2022)
IAPv4	3.52	0.75	0.66 ± 0.04
IAPv3	3.52	0.79	0.56 ± 0.03
ISH	7.49	1.35	0.63 ± 0.05
EN4	8.79	1.03	0.67 ± 0.04
BOA	10.05	1.16	0.60 ± 0.07
NECI	11.29	1.11	0.61 ± 0.07
SIO	10.00	1.24	0.56 ± 0.08
CERES	0.67	0.33	<u>0.77</u>

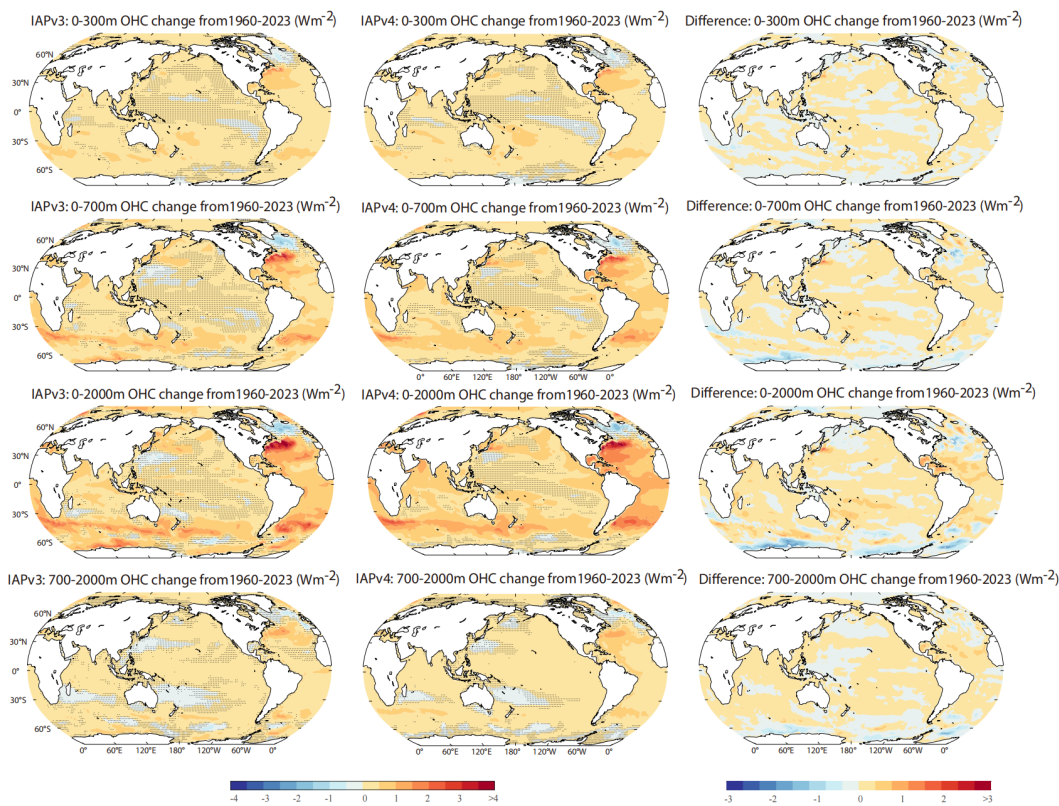
3.5 Regional OHC trends

For 1960–2023 (Fig. 13), the IAPv4 trends are slightly weaker than IAPv3 in the Pacific Ocean but slightly higher in the Atlantic Ocean (Fig. 13), with more than 95 % of the ocean area showing a warming trend. The polar regions also show remarkable differences compared to IAPv3 (Section 3.1), mainly because of the change of covariance, which improves the spatial reconstruction in the polar regions. The IAPv4 shows stronger warming near the boundary currents regions, mainly because of the improved QC that does not flag high-temperature anomalies. Nevertheless, the pattern of trends is very similar in the two versions of data, indicating the robustness of the ocean warming pattern. The Atlantic Ocean (within 50 °S–50 °N) and the Southern Ocean store more heat than the other basins, probably associated with the deep convection and subduction processes

删除了: 2

删除了: 2

817 effectively transporting heat into the deep layers (Cheng et al., 2022a). The cold spots
 818 mainly include the Northwest Pacific and subpolar North Atlantic Ocean. In particular, the
 819 so-called “warming hole” in the subpolar North Atlantic Ocean can extend to at least 800
 820 m and is responsible for decreased OHC in this region. Some studies have linked this
 821 fingerprint to the slowdown of AMOC (Rahmstorf et al, 2015; Caesar et al., 2018).



823 **Figure 13:** Spatial pattern of the OHC trends for 0–300 m, 0–700 m and 0–2000 m,
 824 700–2000 m from 1960 to 2023. The left panels show IAPv3, the middle panels are
 825 IAPv4; the right panels are the difference between IAPv4 and IAPv3.

826 For 1991–2023 (Fig. 14), the IAPv4 and IAPv3 pattern is also consistent. A trend
 827 pattern mimicing a negative Pacific Decadal Variability (PDV) phase appears in the Pacific
 828 for the 0–300 m, 0–700 m, and 0–2000 m OHCs. There is a contrast between the warming

删除了: 2

删除了: 3

删除了: La Niña-like

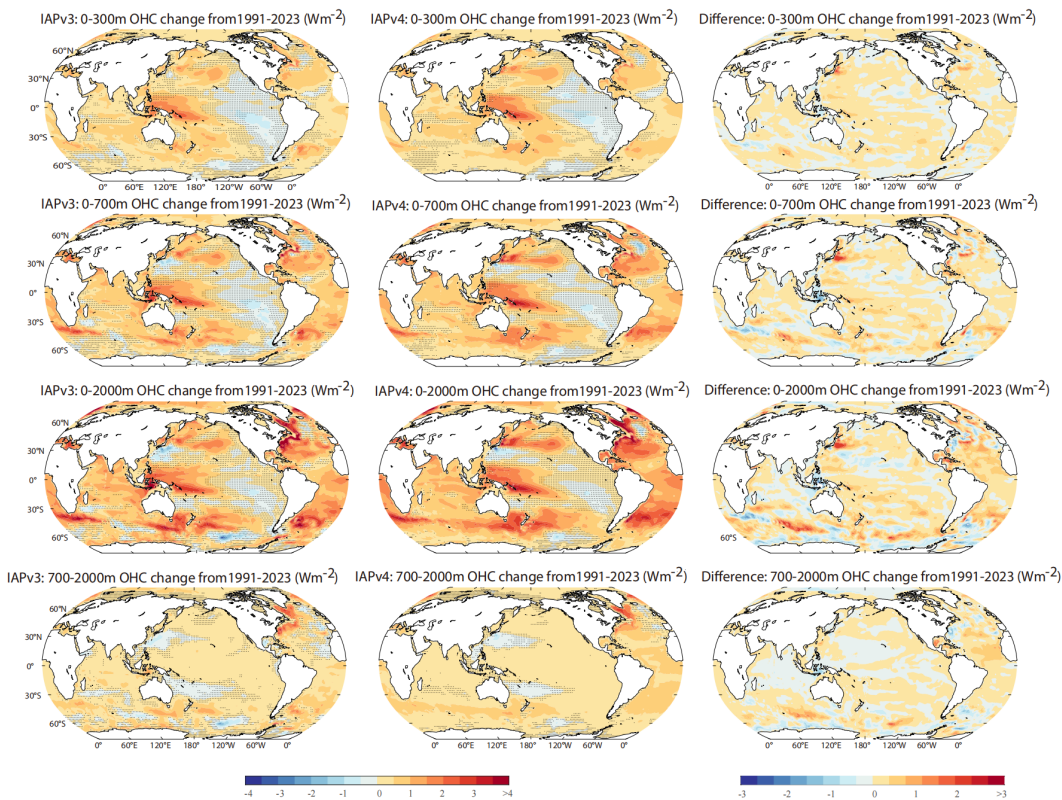
删除了: s

删除了:

834 trend of the tropical western Pacific and the cooling trend of the tropical eastern Pacific.
 835 Some studies have linked this pattern to the natural climate mode (PDV) (England et al.,
 836 2014), but some suggest it is a forced change driven by greenhouse gas increases (Fasullo
 837 and Nerem, 2018; Mann, 2021). Below 700 m, the 1960–2023 and 1991–2023 trend
 838 patterns are similar because deep ocean warming mainly occurs after 1990. Broad warming
 839 in most regions, but subtropical oceans in the West Pacific and South Indian oceans show a
 840 cooling, which is likely related to the subtropical gyre intensification in the North but a
 841 spin-down in the North Pacific Ocean (Zhang et al., 2014).

删除了: Pacific Decadal Variability

删除了: expansion and



843 **Figure 14:** Spatial pattern of the OHC trends for 0–300 m, 0–700 m, 0–2000 m and
 844 700–2000 m from 1991 to 2023. The left panels show IAPv3, the middle panels are
 845 IAPv4; the right panels are the difference between IAPv4 and IAPv3.

删除了: 3

849 Furthermore, the reconstruction of IAPv4 is compared with completely independent
 850 observations in the central Labrador Sea (see Data and Methods section for details;
 851 Yashayaev, 2007; Yashayaev and Loder, 2017) for the 200-2000 m mean temperature time
 852 series (Fig. 15). The direct observations show a substantial decadal variation in the central
 853 Labrador Sea, with negative anomalies 1970-2003 and 2015-2020, and positive anomalies
 854 1963-1972 and 2004-2014. Reconstructed based on data from WOD, IAPv4 can well
 855 represent this decadal variability. The largest difference occurs in 1989, where direct
 856 observations show nearly zero anomaly while IAPv4 shows a big negative anomaly; this
 857 difference is likely caused by using a time window in IAPv4, which has a smoothing effect
 858 on the time series.

设置了格式: 字体颜色: 文字 1
 带格式的: 缩进: 首行缩进: 2 字符

设置了格式: 字体颜色: 文字 1

删除了: within

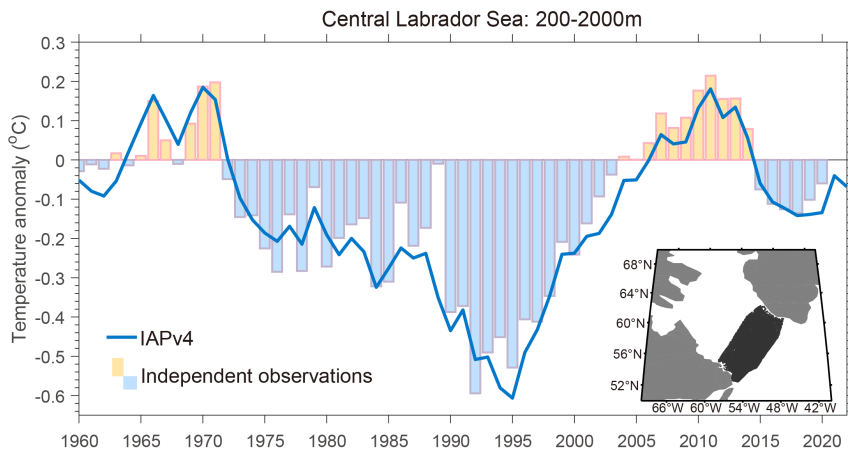
设置了格式: 字体颜色: 文字 1

删除了: within

删除了: might be

删除了: ,

设置了格式: 字体颜色: 文字 1



859 **Figure 15: Comparison of IAPv4 data with independent observations in the central**
 860 **Labrador Sea (304-310 °E, 55-61 °N) from 1960 to 2020. The 200-2000 m averaged**
 861 **temperature anomaly time series is shown, and the baseline is 1960-2020. The inner box**
 862 **shows the locations of the independent observations in black dots (showing a total of**
 863 **49,849 profiles).**

带格式的: 居中

删除了: °E

删除了: °N

设置了格式: 字体: 非加粗

866 3.6 Ocean meridional heat transport

867 The ocean meridional heat transport (MHT) is fundamental to maintaining the earth's
 868 energy balance. Thus, its change and stability are key to the climate system and its
 869 variability. The direct observations of ocean MHT are only possible in several cross-basin
 870 sections such as RAPID. The ocean MHT can be derived from the OHC and air-sea heat

删除了: The ocean accounts for about one-third of t

带格式的: 缩进: 首行缩进: 2 字符, 行距: 1.5 倍行距

删除了: .

删除了: indirectly

880 flux data (Trenberth and Fasullo, 2017; Trenberth et al., 2019) as follows; we integrate the
881 OHC and air-sea heat flux from the North Pole southward in the Atlantic Ocean, and solve
882 the energy budget question, the residual at each latitude is the MHT, i.e.,

$$883 \quad MHT(\varphi) = \int_{\varphi}^{90} \left[F_s + \frac{dOHC}{dt} \right] a d\varphi$$

884 Where a is the Earth's radius, φ is latitude, F_s is net surface heat flux. Both F_s
885 and OHC are important for the MHT derivation: the integrated air-sea heat flux dominates
886 the magnitude of the MHT, while the OHC dominates the variability of the MHT (Liu et
887 al., 2020).

888 The comparison between OHC-derived MHT and RAPID data allows one to check
889 the consistency among various observations. Here, we calculate the Atlantic MHT from
890 April 2004 to December 2022 using IAPv4 OHC and air-sea net heat flux data (F_s) derived
891 by TOA net energy flux and atmospheric heat divergence (Fig. 16). F_s is an average of
892 three available products including MAYER2021 (Mayer et al., 2021) TF2018 (Trenberth et
893 al., 2019) and the DEEP-C Version 5.0 from Reading University (Liu and Allan, 2022; Liu
894 et al., 2020). The data are adjusted following Trenberth et al., (2019) approach to ensure
895 zero MHT on the Antarctica coast. The inferred time series of MHT at 26.5 °N from other
896 OHC data sets (IAPv3, Ishii, and EN4) are also shown in Fig. 16, compared with the
897 RAPID observations (Johns et al., 2023).

898 The Inferred long-term mean (April 2004–December 2022) MHT from the updated
899 IAPv4 OHCT (solid red line with the mean transport of 1.18 PW) is identical to the
900 RAPID observation of 1.18 ± 0.19 PW. Different OHC datasets cause different inter-
901 annual variability in the MHT. It is shown that, from 2008 to 2020, the RAPID MHT
902 agrees best with the IAPv4 estimates with a correlation of 0.52. By comparison, the
903 correlation coefficients between RAPID and IAPv3, EN4, and Ishii are 0.33, 0.51, and
904 0.49, respectively. Over the entire period of 2005~2022, the IAPv4 lies mostly within the
905 RAPID uncertainty envelope.

设置了格式: 字体: (默认) Times New Roman, 12 磅, 字体颜色: 文字 1

设置了格式: 字体: 12 磅, 字体颜色: 文字 1

设置了格式: 字体: 12 磅, 字体颜色: 文字 1

设置了格式: 字体: 12 磅, 字体颜色: 文字 1

设置了格式: 字体: 12 磅, 字体颜色: 文字 1

设置了格式: 字体: 12 磅, 字体颜色: 文字 1

设置了格式: 字体: 12 磅, 字体颜色: 文字 1

设置了格式: 字体: 12 磅, 字体颜色: 文字 1

设置了格式: 字体: 12 磅, 字体颜色: 文字 1

设置了格式: 字体: 12 磅, 字体颜色: 文字 1

设置了格式: 字体: 12 磅, 字体颜色: 文字 1

设置了格式: 字体: (默认) Times New Roman, 12 磅, 字体颜色: 文字 1

设置了格式: 字体: 12 磅, 字体颜色: 文字 1

设置了格式: 字体: (默认) Times New Roman, 12 磅, 字体颜色: 文字 1

设置了格式: 字体: 12 磅, 字体颜色: 文字 1

设置了格式: 字体: (默认) Times New Roman, 12 磅, 字体颜色: 文字 1

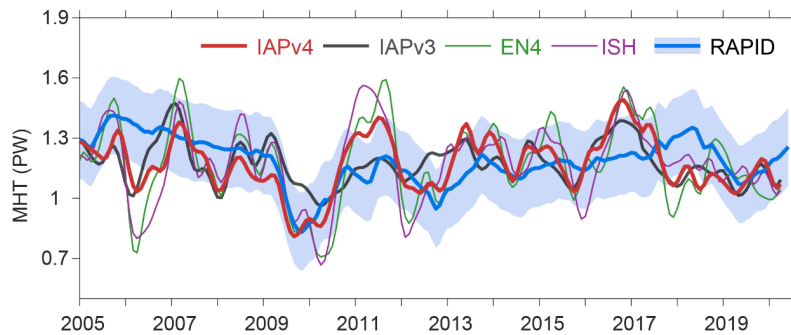
设置了格式: 字体: 12 磅, 字体颜色: 文字 1

设置了格式: 字体: (默认) Times New Roman, 12 磅, 字体颜色: 文字 1

删除了: 4

删除了: ,

删除了: 4



909

910 **Figure 16: Derived Meridional heat transport at 26.5 °N.** The 12-month running mean
 911 northward MHT across 26.5 °N of different data sets compared with results from the
 912 RAPID array in PW. The error bars for RAPID in grey are 1.64 σ .

删除了: 4

913

914 3.7 Inter-annual variability

915 The year-to-year variation of OHC is strongly influenced by ENSO from global to
 916 regional scales (Cheng et al., 2019; Roemmich and Gilson, 2011). To demonstrate the
 917 change of OHC associated ENSO, Figure 17 shows a Hovmöller diagram of the zonal
 918 upper 2000 m OHC and its change (time derivative of OHC: $d(\text{OHC})/dt$) in the tropical
 919 Pacific Ocean from 1985 to 2023, compared with the Oceanic Niño Index (ONI). It is
 920 evident that both OHC and OHCT are closely correlated with ENSO.

删除了: 5

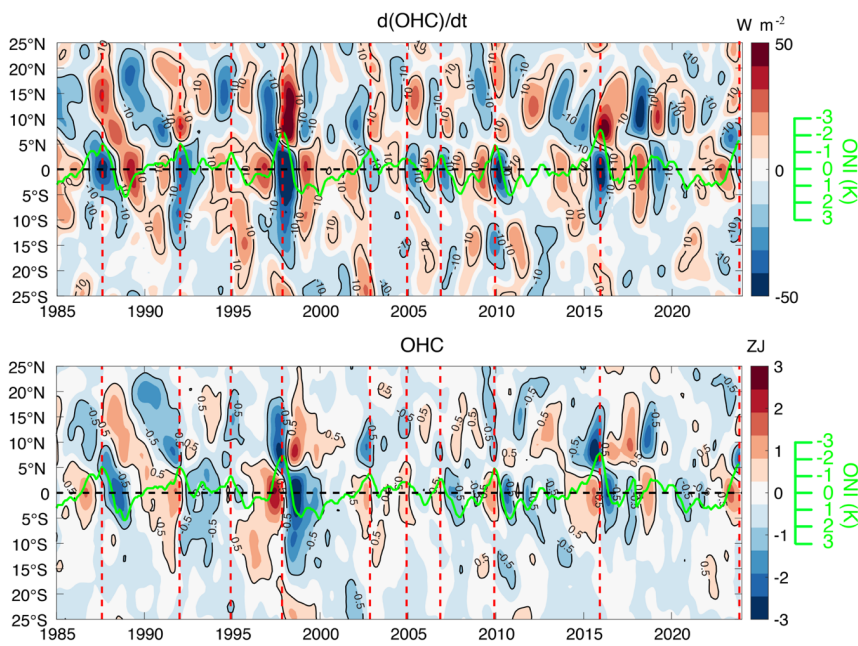
921 Before the onset of El Niño events, there is an accumulation of heat ($d(\text{OHC})/dt > 0$)
 922 in the southern and equatorial tropical Pacific ocean region (20 °S– 5 °N). The positive
 923 tropical Pacific $d\text{OHC}/dt$ leads ONI by ~15 months (with peak correlation >0.5), making it
 924 a precursor of El Niño (Cane and Zebiak 1985; McPhaden, 2012; Lian et al., 2023). In
 925 contrast, heat is redistributed ($d(\text{OHC})/dt < 0$) from the tropical Pacific (20 °S – 5 °N) to
 926 the North Pacific (5 °N – 25 °N) during and after El Niño (Cheng et al., 2019), with a
 927 maximum correlation >0.8 at 5 months after the El Niño peak. The magnitude of the
 928 prominent change can reach up to 50 Wm^{-2} during the 1997–1998 and 2015–2016 extreme
 929 El Niño events. For the other moderate El Niño events, the regional Pacific OHC change
 930 varies around 10–20 Wm^{-2} (Mayer et al., 2018). This typical heat recharge-discharge
 931 paradigm is crucial in ENSO evolution (Jin, 1997). Correspondingly, the zonal OHC
 932 anomalies in the Pacific Ocean show a warming state ($\text{OHC} > 0$) between ~20 °N and
 933 ~5 °S before the peak of El Niño events (with peak correlation >0.7 at 5 months before El

删除了: released

删除了: s

删除了: Hemisphere

939 Niño peak), followed by a period of cooling (OHC < 0) after the peak of El Niño (with
 940 peak correlation >0.7 at 12 months after El Niño peak). These variations are all physically
 941 meaningful and indicate that IAPv4 represents regional inter-annual variability, especially
 942 associated with ENSO.



943
 944 **Figure 17:** Hovmöller diagrams illustrating the zonal mean (top) upper 2000 m d(OHC)/dt
 945 (Wm⁻²) and (bottom) OHC (ZJ) in each 1 ° latitude band within 25 °S ~ 25 °N in the
 946 tropical Pacific basin using IAPv4 data. The ONI is shown in green. Vertical dashed lines
 947 denote the peak time of each Niño event.

删除了: 5

948

949 3.8 Ocean and Earth Energy Budget

950 The EEI provides a critical quantifier of the Earth's energy flow and climate change.
 951 It is also policy-relevant because it clearly shows the need to stabilize the climate system.
 952 With new T/OHC data, we re-assess the Earth's energy inventory since 1960. The land,
 953 atmosphere, and ice contributions are from the estimates obtained by von Schuckmann et
 954 al. (2023) for 1960-2023 and by Trenberth (2022) for 2015-2019.

956 It is evident that the earth has been accumulating heat since 1960. The Earth's heat
 957 inventory is 524.0 ± 95.6 ZJ from 1960 to 2023 and 260.3 ± 25.3 ZJ from 2005–2023
 958 based on our data. The upper 700 m ocean, 700–2000 m, 2000 m-bottom, land, ice, and
 959 atmosphere contribute to 59.3%, 24.1%, 7.4%, 5.2%, 2.9%, and 1.1% of the total EEI,
 960 respectively, since 1960. The relative contribution has changed with time; for instance,
 961 since 1993, the contributions are 53.7% (0–700 m ocean), 24.8% (700–2000 m ocean),
 962 12.8% (2000 m–bottom ocean), 4.1% (land), 3.2% (ice), and 1.4% (atmosphere). The land
 963 and ice contribution has increased in the recent two decades because of accelerated land
 964 and sea ice melting (Comiso et al., 2017; Hugonnet et al., 2021; Minière et al., 2024).
 965 From 2005–2019, more reliable land–atmosphere–ice datasets in Trenberth (2022) suggest
 966 a non–ocean contribution of 13.4 ZJ. Combined with the results for OHC with IAPv4, the
 967 accumulated EEI is 182.5 ZJ with the ocean heat uptake of 169.1 ± 19.7 for 2005–19,
 968 consistent with the value of 186.4 ± 23.1 ZJ using the non–ocean contribution data by von
 969 Schuckmann et al. (2023).

970 The derived energy inventory has been compared with satellite–based observations at
 971 the top of the atmosphere (TOA). Two comparisons are made: (1) integrate the TOA EEI
 972 to compare with the energy inventory (Fig. 18); (2) take the time derivative of the annual
 973 OHC to compare it with the TOA net radiation flux (Fig. 19). Here we always assume 90%
 974 of EEI is stored in the ocean and leads to an increase of OHC (Trenberth et al. 2009;
 975 Hansen et al., 2011; von Schuckmann et al., 2020).

976 The first approach avoids calculating the time derivative of OHC, which exacerbates
 977 noise in the time series. The net CERES change has been adjusted to 0.71 Wm^{-2} within
 978 2005–2015, here we adjust the trend of the integrated CERES data to the IAPv4 OHC
 979 trend to make it consistent and then compare the variability difference (Fig. 18). The
 980 RMSE between DeepC and IAPv4 is 17.9 ZJ and 15.5 ZJ between CERES and IAPv4. The
 981 comparison also indicates that the heat inventory shows a stronger heat increase from 2000
 982 to 2005 but too slow heat accumulation during 2005–2010 compared with DeepC and
 983 CERES (Fig. 18). This might be due to the data gaps before the Argo network was fully
 984 established. DeepC and CERES show stronger heat accumulation since ~2015 than the
 985 heat inventory, probably associated with the accelerated abyssal ocean warming found by
 986 the Deep-Argo program (Johnson et al., 2019). Furthermore, IAPv4 OHC shows a slightly
 987 higher (but consistent within the uncertainty range) Earth's heat uptake compared to von

- 删除了: 57.9
- 删除了: 512.9 ± 65.0
- 删除了: 15.3
- 删除了: $251.5 \pm 14 \text{ ZJ}$
- 删除了: 56.5%, 25.7%, 9.2%, 4.8%, 2.7%,
- 删除了: 55.2%
- 删除了: 22.1
- 删除了: 11.7
- 删除了: 3.7
- 删除了: 2.8
- 删除了: 0

- 删除了: 188.7
- 删除了: 12
- 删除了: 175.3 ± 11
- 删除了:
- 删除了: 14
- 删除了: 192.2 ± 12

- 删除了: 6
- 删除了: 7

- 删除了: 6
- 删除了: The RMSE between DeepC and IAP–OHC is 18.3 ZJ and 16.1 ZJ for CERES versus IAP–OHC.

- 删除了: 6

1011 Schuckmann et al. (2023) results by 76.2 ZJ from 1960 to 2020, mainly because the
1012 correction of Nansen bottle biases and the updates of XBT and MBT biases in IAPv4 data.

删除了: 33.5

1013 The second approach to compare OHC with satellite-based EEI is to calculate the
1014 time derivative of OHC. To suppress the month-to-month noises, we estimate annual
1015 OHC based on one-year data centered on June (Fig. 19a) and December (Fig. 19b)
1016 separately, and then $dOHC/dt$ is calculated with a forward derivative approach based on
1017 the annual time series. The annual mean of EEI time series is also used here for
1018 comparison (Fig. 19). The IAPv4 and CERES estimates show inter-annual variability with
1019 a correlation of 0.44. The higher correlation of IAPv4 versus CERES than IAPv3 increases
1020 confidence for the new data (correlation of only ~ 0.15 for IAPv3). The trend of $dOHC/dt$ is
1021 $0.36 \text{ Wm}^{-2} \text{ dec}^{-1}$ from 2005 to 2023, within the uncertainty range of the CERES record
1022 ($0.50 \pm 0.47 \text{ Wm}^{-2} \text{ dec}^{-1}$ in Loeb et al., 2021). However, it should be noted that the
1023 calculation of $dOHC/dt$ is sensitive to the choices of methods, data products, and time
1024 periods because of the noises and variability in the OHC time series. A careful analysis of
1025 the trend of $dOHC/dt$ (and EEI) is a research priority.

删除了: 7

删除了: 7

删除了: 7

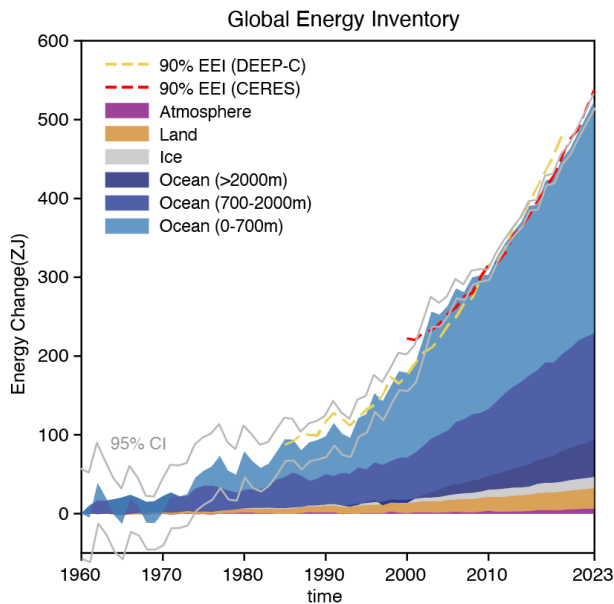
删除了: consistent

删除了: consistency

删除了: gives higher

删除了: IAPv4

删除了: than IAPv3

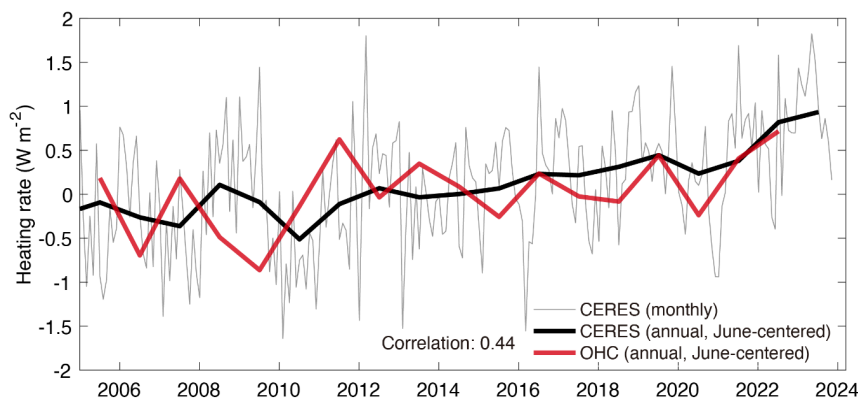


1026
1027 **Figure 18:** The global energy budget from 1960 to 2023. The Atmosphere, land, and ice
1028 heat inventory is from von Schuckmann et al., (2023). Integrated EEI from DEEP-C
1029 (1985–2018) (Liu and Allan, 2022) and CERES (2001–2023) (Loeb et al., 2021) dataset

删除了: 6

删除了: 2

1041 are presented by dashed lines for comparison, with the trend adjusted to the IAP estimate
 1042 to account for the arbitrary choice of integration constant. 95% Confidence Interval is
 1043 presented assuming the independency of different budget components.
 1044



1045
 1046 **Figure 19: Annual ocean heating rate compared with CERES data.** Both annual OHC
 1047 and CERES EEI data are centred in June. The long-term mean is removed for all-time
 1048 series.
 1049

1050 **3.9 Steric sea level and sea level budget**

1051 The updated IAPv4 data is used to assess the sea level budget for 1960-2023 in
 1052 combination with other data, including IAP salinity data, glaciers, Greenland, Antarctic ice
 1053 sheets mass loss from Frederikse et al. (2020) and altimetry sea level record (see Methods
 1054 section for details). From 1960 to 2023, the observed GMSL rise is $2.07 \pm 0.55 \text{ mm yr}^{-1}$,
 1055 and the sum of contributions yields a mean sea level rise of $1.87 \pm 0.42 \text{ mm yr}^{-1}$. Thus,
 1056 the sea level budget can be closed within a 90% confidence interval. This updated estimate
 1057 indicates that the steric sea level, Antarctic ice sheet, Greenland ice sheet, glaciers, and
 1058 land water storage contribute to the total sea level with 47.3%, 8.6%, 18.0%, 29.1%, and -
 1059 3.1%, respectively for 1960-2023.

1060 To isolate the contribution of the IAPv4 to the sea level budget, we replace the steric
 1061 sea level estimate in Frederikse et al., (2020) with IAPv4 and re-assess the sea level budget
 1062 for 1960-2018, 1993-2018 and 2005-2018, and the other components are identical to
 1063 Frederikse et al., (2020). Two metrics are used to quantify the performance of sea level

删除了: 7

删除了: ered o

删除了: 2.1

删除了: 0.5

删除了: 1.9

删除了: 0.4

设置了格式: 上标

设置了格式: 字体: (默认) Times New Roman

带格式的: 缩进: 首行缩进: 2 字符

删除了: exactly the same

删除了: as in

删除了: ,

1073 budget closure: the mean residual error and the root mean square error (RMSD) between
1074 the observed GMSL and the sum of contributions. We find that the residual sea level
1075 budget based on IAPv4 is 0.20 ± 0.53 , 0.11 ± 0.34 , 0.47 ± 0.56 mm yr⁻¹ for 1960-2018,
1076 1993-2018 and 2005-2018, respectively. These mean residual errors are all smaller than
1077 presented in Frederikse et al., (2020), which showed a residual error of 0.29 ± 0.57 , $0.20 \pm$
1078 0.34 and 0.54 ± 0.58 mm yr⁻¹ for 1960-2018, 1993-2018 and 2005-2018, respectively. The
1079 RMSD using IAPv4 (or using steric sea level in Frederikse et al., 2020) is 5.59 (5.35), 4.89
1080 (5.33) and 4.21 (4.51) mm for the above-mentioned three periods, respectively. Therefore,
1081 both metrics show that IAPv4 data improves the sea level budget in three typical periods.

删除了: that

删除了: ing

1082 A similar test is done with the IPCC-AR6 sea level budget estimate (Gulev et al.,
1083 2021): the thermosteric sea level estimate in IPCC-AR6 is replaced by IAPv4, and the sea
1084 level budget is re-assessed for 1993-2018. IAPv4 suggests a larger thermosteric sea level
1085 rise of 1.43 ± 0.16 for 1993-2018 than IPCC (1.31 ± 0.36 mm yr⁻¹) from 1993-2018.
1086 Replacing the thermosteric sea level estimate by IAPv4 reduces the mean residual error
1087 from 0.40 ± 0.57 to 0.28 ± 0.48 mm yr⁻¹. This suggests again that the stronger warming
1088 since the 1993, revealed by IAPv4, seems more realistic.

删除了: 1960s

删除了: , as

删除了: **Table 3. Sea level budget is based on IAPv4 and previous studies.** The trends of IPCC AR6 and (Frederikse et al., 2020) are based on least-squares fit. The trend of IAPv4 is based on LOWESS method (Cheng et al., 2022b). The uncertainty of IPCC AR6 and Frederikse et al. (2020) is given by the 90% confidence interval. The uncertainty of IAPv4 is based on a 90% confidence interval through the Monte Carlo method. The unit is mm yr⁻¹. ... [1]

1090 After 2002, the GRACE satellite supported the direct observation of barystatic sea
1091 level, which is the sum of the sea level change due to the land water storage, Antarctica ice
1092 sheet, Greenland ice sheet, and glaciers. The sea level budget can be obtained by
1093 comparing altimetry-based GMSL with the barystatic sea level observed by GRACE and
1094 the steric sea level. It is evident that the sea level budget can be closed between 2002 and
1095 2015 with ± 5 mm residual errors (Fig. 20b). However, after ~2015, the sum of steric and
1096 barystatic sea level is smaller than the total sea level rise for all ocean temperature
1097 products. Previous studies have attributed this misclosure to salinity data biases (Barnoud
1098 et al., 2021), altimetry data errors (Barnoud et al., 2023), and GRACE data errors (Wang et
1099 al., 2021). The steric sea level inferred from IAPv4 showed a lower residual (~5 mm)
1100 between 2005–2023 than ISH and EN4 data (10~20 mm), indicating that the temperature
1101 data might be partly responsible for lack of closure of sea level budget since ~2015. This
1102 suggests that the stronger warming in recent years, as indicated by IAPv4, is more realistic.
1103 As discussed in Section 3.4, the QC is mainly responsible for the increased warming of
1104 IAPv4 compared with IAPv3 since ~2015 (Fig. 11).

删除了: 18

删除了: seem

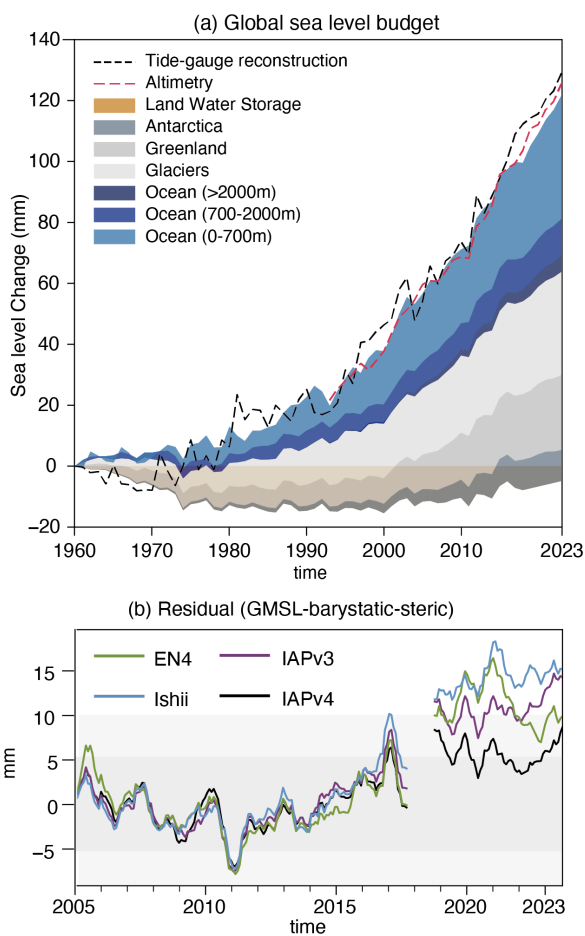
1105 Many traditional QC procedures use a static climatological range check to filter out
1106 outliers, which does not account for the increase of extreme events with climate change

删除了: d

1122
1123
1124
1125
1126
1127

and removes too many extreme (positive) values during the recent period. Thus, we strongly recommend that data product generation groups revisit the QC procedure. Furthermore, as the stronger long-term OHC trends since ~1960 in IAPv4 than in IAPv3 are mainly attributed to the bias corrections for Nansen Bottle, MBT, and XBT data, it is also recommended that international groups to revisit the biases in ocean observations.

删除了: might
删除了: e
删除了: thus



1128

1129 **Figure 20:** (a) The sea level budget from 1960 to 2023. Observed global mean sea level
1130 for 1960–2023, and the individual contributions from land water storage, Antarctica,
1131 Greenland and Glaciers (Frederikse et al., 2020). The budget is relative to a 1960 baseline.
1132 Here, the land water storage and Glaciers data are through 2018, and a linear extrapolation

删除了: 18
删除了: 1
删除了: 1
删除了: 1959–1961
删除了: Antarctica, Greenland, and

1141 is made for 2019–2023. [Antarctica ice sheet and Greenland ice sheet changes are](#) estimated
1142 by GRACE after 2018. [Tide gauge after 2018 are updated by altimetry](#). Altimetry sea level
1143 is shown in red dashed line for comparison. (b) Sea level budget residual time series since
1144 2005. The residual of GMSL minus barystatic and steric sea level. The seasonal cycle is
1145 reduced based on 2005–2015 climatology. A 6–month [running smooth](#) is applied to reduce
1146 the noise.

删除了： 2021

删除了： Land water storage

删除了： is

删除了： A

删除了： lowpass

删除了： filter

1147

1148 4. Data availability

1149 IAPv4 global ocean temperature product is available at
1150 <http://dx.doi.org/10.12157/IOCAS.20240117.002> (Cheng et al., 2024a) and
1151 <http://www.ocean.iap.ac.cn/>.

1152 IAPv4 global ocean heat content product is available at
1153 <http://dx.doi.org/10.12157/IOCAS.20240117.001> (Cheng et al., 2024b) and
1154 <http://www.ocean.iap.ac.cn/>.

1155 The code used in this paper includes data quality control, and the resultant dataset is
1156 available at <http://www.ocean.iap.ac.cn/>.

1157

1158 The data used in this study (but not generated by this work) are listed below. IAP data are
1159 available at <http://www.ocean.iap.ac.cn/>. The NCEI/NOAA data are available at
1160 (<https://www.ncei.noaa.gov/products/climate-data-records/global-ocean-heat-content>). ISH
1161 data from (<https://climate.mri-jma.go.jp/pub/ocean/ts/v7.2/>). The EN4 data
1162 (<https://www.metoffice.gov.uk/hadobs/en4/index.html>) For SST: ERSSTv5
1163 (<https://www1.ncdc.noaa.gov/pub/data/cmb/ersst/v5/netcdf/>); COBE2
1164 (<https://psl.noaa.gov/data/gridded/data.cobe2.html>); and HadSST3
1165 (<https://www.metoffice.gov.uk/hadobs/hadsst3/data/download.html>). For sea level data:
1166 AVISO+ GMSL ([https://www.aviso.altimetry.fr/en/data/products/ocean-indicators-
1167 products/mean-sea-level.html#c15723](https://www.aviso.altimetry.fr/en/data/products/ocean-indicators-products/mean-sea-level.html#c15723)), [JPL GRACE](https://grace.jpl.nasa.gov/data/get-data/jpl_global_mascons/) ([https://grace.jpl.nasa.gov/data/get-
1168 data/jpl_global_mascons/](https://grace.jpl.nasa.gov/data/get-data/jpl_global_mascons/)), the data in Frederikse et al., (2020) from
1169 (<https://zenodo.org/records/3862995>). The data in von Schuckmann et al., (2023)
1170 (https://www.wdc-climate.de/ui/entry?acronym=GCOS_EHI_1960-2020). Argo data were
1171 collected and made freely available by the International Argo Program and the national
1172 programs that contribute to it (<https://argo.ucsd.edu>, <https://www.ocean-ops.org>). DEEP-C
1173 data from <https://doi.org/10.17864/1947.000347>; CERES data ([删除了： CSR GRACE \(<https://www2.csr.utexas.edu/grace/>\)](https://ceres-</p></div><div data-bbox=)

1181 tool.larc.nasa.gov/ord-tool/jsp/EBAFTOA41Selection.jsp); PIOMAS ice volume data from
1182 (<http://psc.apl.uw.edu/research/projects/arctic-sea-ice-volumeanomaly/>). SCRIPPS data
1183 from (http://sio-argo.ucsd.edu/RG_Climatology.html); BOA data from
1184 (<https://argo.ucsd.edu/data/argo-data-products/>).
1185

1186 5. Summary and Discussion

1187 This paper introduces a new version of the ocean temperature and heat content
1188 gridded products and describes the data source and data processing techniques in detail.

1189 The key technical advances include the new QC, new or updated XBT/MBT/Bottle/APB
1190 bias corrections, new ocean temperature climatology, improved mapping approach, and
1191 grid-cell ocean volume corrections. These data and technical advances allow a better
1192 estimate of long-term ocean temperature and heat content changes since the mid-1950s
1193 from the sea surface down to 2000 m. We show that the new data product could better
1194 close the sea level and energy budgets than IAPv3. For rates of change, compared with
1195 CERES, the IAPv4 also shows a better correlation from 2005 to 2023 than IAPv3.

1196 Despite several marked improvements, issues needing further investigation remain.
1197 Although inter-annual and decadal-scale changes of satellite-based EEI and observational
1198 OHC are generally consistent, a mismatch remains between EEI and OHC for their month-
1199 to-month variation, as the monthly variation of OHC is still much larger than implied by
1200 EEI. There are several possibilities, in our opinion: first, there is substantial heat storage
1201 and release for land and ice monthly, which needs to be accurately quantified; second, the
1202 accuracy of OHC estimate on a monthly basis still needs to be improved for month-to-
1203 month variation because of the limited data coverage; third, the EEI observed by CERES
1204 also suffers from sampling biases on a monthly basis (Loeb et al., 2009). Thus, a better
1205 understanding of the monthly variation of OHC and EEI is still a research priority. Besides,
1206 the failure to close the 2015-2023 sea level budget indicates that the underlying data still
1207 has bias problems, which need to be explored and resolved.

1208 Second, the application of CODC-QC in IAPv4 leads to a stronger ocean warming
1209 rate in the past decade than WOD-QC used in IAPv3 because WOD-QC removes more
1210 positive temperature anomalies than CODC-QC. This could imply that the rate of increase
1211 in OHC is still slightly underestimated and deserves an in-depth investigation. Several
1212 fundamental questions must be answered: first, are there still real temperature extremes
1213 being removed by CODC-QC, such as in small warm/cold eddies? Are the extremes well

删除了: d

删除了: d

1216 sampled by the current observation system? If not, what is the impact? Moreover, it is clear
1217 that the high latitudes where sea ice occurs are not well sampled and need more attention.

1218 Third, during the development of the data product, we discovered that much metadata
1219 relating to the profiles in the World Ocean Database is missing and that much existing
1220 metadata is incorrect, also giving rise to duplicate profiles, putting a strain on the overall
1221 quality of a database of oceanic observations. More than ever, long-term concerted efforts
1222 are needed to eliminate duplicate profiles and identify and correct missing metadata using
1223 statistical methods, expert control, or machine learning techniques. For example, the
1224 International Quality-Controlled Database (IQuOD) group is coordinating some activities
1225 related to data processing techniques, uncertainty quantification, and improving the overall
1226 quality of ocean data (Cowley et al., 2021).

1227 Fourth, the deep ocean changes below 2000 m are estimated based on the currently
1228 available data, including data from hydrological sections and Deep-Argo. IAP mapping
1229 technique is applied. Because of the lack of independent observations with global ocean
1230 coverage, evaluating the deep ocean change estimate is still dicey. Thus, the below-2000 m
1231 estimate should be used with caution, as also indicated in previous estimates (Purkey and
1232 Johnson, 2010; Desbruyères et al., 2017; Good et al., 2013). A community-agreed
1233 evaluation approach for the deep ocean changes is critically needed. Besides, other
1234 mapping techniques deserving further investigation include interpolation on isopycnal
1235 surfaces (Palmer and Haines, 2009).

1236 Furthermore, the quantification of uncertainty for *in situ* measurements, gridded
1237 T/OHC values, and the global OHC estimates need to be improved. IAPv4 only accounts
1238 for the instrumental error and sampling/mapping error. In the future, comprehensive
1239 quantification of other uncertainty sources will be made, including the choice of
1240 climatology, vertical interpolation, XBT/MBT/APB/Bottle corrections, etc. It is also
1241 necessary to analyze the correlation between these error sources. This also helps to
1242 understand regions with larger uncertainty for OHC estimates, which supports the design
1243 of the global ocean observing system.

1244
1245 **Author contributions.** L.C. has worked on this study's conceptualization, coordination,
1246 methodologies, and writing the manuscript. Z.T. worked on *in situ* observation collections,
1247 metadata format, and the automated quality control procedure (CODC-QC) development.
1248 Y.P. has worked on calculating and comparing the OHC annual cycle, the mixed layer

删除了: i

删除了: an open issue

设置了格式: 字体: (默认) Times New Roman, 12 磅

设置了格式: 字体: (默认) Times New Roman, 12 磅

设置了格式: 字体: (默认) Times New Roman, 12 磅

删除了: e

删除了: , such as

1253 depth, and the MHT among different data sets. V.G. worked on bias correction schemes for
1254 MBT, APB, and bottle data and on developing the automated quality control procedure.
1255 H.Y. worked on the analysis of inter-annual variability. J.D. has worked on OHC trend
1256 calculation and analysis. G.L. worked on SST calculation and its analysis. H. Z. worked on
1257 global energy and sea level budget calculations and analyses. Y.L. and Y.J. worked on the
1258 volume correction. All authors have contributed to formal analysis, data validation, and
1259 editing of the original draft.

1260

1261 **Acknowledgement and Funding.** The IAP/CAS analysis is supported by the National
1262 Natural Science Foundation of China (Grant no. 42122046, 42076202, 42206208,
1263 42261134536), Strategic Priority Research Program of the Chinese Academy of Sciences
1264 (Grant no. XDB42040402), the new Cornerstone Science Foundation through the
1265 XPLORER PRIZE, DAMO Academy Young Fellow, Youth Innovation Promotion
1266 Association, Chinese Academy of Sciences, National Key Scientific and Technological
1267 Infrastructure project “Earth System Science Numerical Simulator Facility” (EarthLab),
1268 the Young Talent Support Project of Guangzhou Association for Science and Technology.
1269 The calculations in this study were carried out on the ORISE Supercomputer. Some data
1270 were collected onboard of R/V Shiyan 6 implementing the Open Research Cruise
1271 NORC2022-10+NORC2022-303 supported by NSFC Shiptime Sharing Projects
1272 42149910. NCAR is sponsored by the US National Science Foundation. We acknowledge
1273 the World Climate Research Programme’s Working Group on Coupled Modelling, which
1274 is responsible for CMIP, and we thank the climate modeling groups for producing and
1275 making their model output available through the Earth System Grid Federation. The Argo
1276 Program is part of the Global Ocean Observing System.

1277

1278 **Competing interests.** The contact author has declared that none of the authors has any
1279 competing interests.

1280

1281 **References**

1282 Abraham, J. P., Cheng, L., Mann, M. E., Trenberth, K., and von Schuckmann, K.: The
1283 ocean response to climate change guides both adaptation and mitigation efforts.

1284 Atmospheric and Oceanic Science Letters, 15, 100221,
1285 <https://doi.org/10.1016/j.aosl.2022.100221>, 2022.

1286 Abraham, J. P., and Cheng, L.: Intersection of Climate Change, Energy, and Adaptation.
1287 Energies. 15(16), 5886; <https://doi.org/10.3390/en15165886>, 2022.

1288 Abraham, J. P., Baringer, M., Bindoff, N. L., Boyer, T., Cheng, L. J., Church, J. A.,
1289 Conroy, J. L., Domingues, C. M., Fasullo, J. T., Gilson, J., Goni, G., Good, S. A.,
1290 Gorman, J. M., Gouretski, V., Ishii, M., Johnson, G. C., Kizu, S., Lyman, J. M.,
1291 Macdonald, A. M., Minkowycz, W. J., Moffitt, S. E., Palmer, M. D., Piola, A. R.,
1292 Reseghetti, F., Schuckmann, K., Trenberth, K. E., Velicogna, I., and Willis, J. K.: A
1293 review of global ocean temperature observations: Implications for ocean heat content
1294 estimates and climate change, *Rev. Geophys.*, 51, 450–483,
1295 <https://doi.org/10.1002/rog.20022>, 2013.

1296 Argo: Argo float data and metadata from Global Data Assembly Centre (Argo GDAC).
1297 SEANOE, 2000.

1298 Bagnell, A., and DeVries, T.: 20(th) century cooling of the deep ocean contributed to
1299 delayed acceleration of Earth's energy imbalance. *Nat. Comm.*, 12, 4604,
1300 <https://doi.org/10.1038/s41467-021-24472-3>, 2021.

1301 Barker, P. M., and McDougall, T. J.: Two Interpolation Methods Using Multiply-Rotated
1302 Piecewise Cubic Hermite Interpolating Polynomials. *J. Atmos. Ocean Technol.*, 37,
1303 605-619, <https://doi.org/10.1175/JTECH-D-19-0211.1>, 2020.

1304 Barnoud, A., Pfeffer, J., Cazenave, A., Fraudeau, R., Rousseau, V., and Ablain, M.:
1305 Revisiting the global mean ocean mass budget over 2005–2020. *Ocean Science*, 19,
1306 321-334, <https://doi.org/10.5194/os-19-321-2023>, 2023.

1307 Barnoud, A., Pfeffer, J., Guérou, A., Frery, M.-L., Siméon, M., Cazenave, A., Chen, J.,
1308 Llovel, W., Thierry, V., Legeais, J.-F., and Ablain, M.: Contributions of Altimetry
1309 and Argo to Non-Closure of the Global Mean Sea Level Budget Since 2016.
1310 *Geophys Res Lett*, 48, e2021GL092824, <https://doi.org/10.1029/2021GL092824>,
1311 2021.

1312 Bindoff, N. L., Cheung, W. W. L., Kairo, J. G., Aristegui, J., Guinder, V. A., Hallberg, R.,
1313 Hilmi, N., Jiao, N., and Karim, M. S.: Changing Ocean, Marine Ecosystems, and
1314 Dependent Communities. In IPCC Special Report on the Ocean and Cryosphere in a
1315 Changing Climate [H.-O. Pörtner, D.C. Roberts, V. Masson-Delmotte, P. Zhai, M.
1316 Tignor, E. Poloczanska, K. Mintenbeck, A. Alegria, M. Nicolai, A. Okem, J. Petzold,
1317 B. Rama, N.M. Weyer (eds.)], Cambridge University Press, Cambridge, UK and

1318 New York, NY, USA, pp. 447–587. <https://doi.org/10.1017/9781009157964.007>,
1319 2019.

1320 Boyer, T., Domingues, C. M., Good, S. A., Johnson, G. C., Lyman, J. M., Ishii, M.,
1321 Gouretski, V., Willis, J. K., Antonov, J., Wijffels, S., Church, J. A., Cowley, R., and
1322 Bindoff, N. L.: Sensitivity of Global Upper Ocean Heat Content Estimates to
1323 Mapping Methods, XBT Bias Corrections, and Baseline Climatologies, *J. Climate*,
1324 29, 4817–4842, <https://doi.org/10.1175/JCLI-D-15-0801.1>, 2016.

1325 Caesar, L., Rahmstorf, S., Robinson, A., Feulner, G., and Saba, V.: Observed fingerprint of
1326 a weakening Atlantic Ocean overturning circulation. *Nature*, 556, 191–196,
1327 <https://doi.org/10.1038/s41586-018-0006-5>, 2018.

1328 Cane, M. A., and Zebiak, S. E.: A theory for El Niño and the southern oscillation. *Science*,
1329 228, 1085–1087, <https://doi.org/10.1126/science.228.4703.1085>, 1985.

1330 Cheng, L.: Sensitivity of Ocean Heat Content to Various Instrumental Platforms in Global
1331 Ocean Observing System. *Ocean-Land-Atmosphere Research*, 0,
1332 <https://doi.org/10.34133/olar.0037>, 2024a.

1333 Cheng, L., and Zhu, J.: Uncertainties of the Ocean Heat Content Estimation Induced by
1334 Insufficient Vertical Resolution of Historical Ocean Subsurface Observations. *J.*
1335 *Atmos. Ocean Technol.*, 31, 1383–1396, [https://doi.org/10.1175/JTECH-D-13-](https://doi.org/10.1175/JTECH-D-13-00220.1)
1336 00220.1, 2014.

1337 Cheng, L., and Zhu, J.: Influences of the Choice of Climatology on Ocean Heat Content
1338 Estimation. *J. Atmos. Ocean Technol.*, 32, 388–394, [https://doi.org/10.1175/JTECH-](https://doi.org/10.1175/JTECH-D-14-00169.1)
1339 D-14-00169.1, 2015.

1340 Cheng, L., and Zhu, J.: Benefits of CMIP5 Multimodel Ensemble in Reconstructing
1341 Historical Ocean Subsurface Temperature Variations. *J. Climate*, 29, 5393–5416,
1342 <https://doi.org/10.1175/JCLI-D-15-0730.1>, 2016.

1343 Cheng, L., Zhu, J., Cowley, R., Boyer, T., and Wijffels, S.: Time, Probe Type, and
1344 Temperature Variable Bias Corrections to Historical Expendable Bathythermograph
1345 Observations. *J. Atmos. Ocean. Technol.*, 31, 1793–1825,
1346 <https://doi.org/10.1175/jtech-d-13-00197.1>, 2014.

1347 Cheng, L., Abraham, J., Goni, G., Boyer, T., Wijffels, S., Cowley, R., Gouretski, V.,
1348 Reseghetti, F., Kizu, S., Dong, S., Bringas, F., Goes, M., Houpert, L., Sprintall, J.,
1349 and Zhu, J.: XBT Science: Assessment of Instrumental Biases and Errors, *B. Am.*
1350 *Meteorol. Soc.*, 97, 924–933, <https://doi.org/10.1175/BAMS-D-15-00031.1>, 2016.

1351 Cheng, L., Trenberth, K. E., Fasullo, J., Boyer, T., Abraham, J., and Zhu, J.: Improved
1352 estimates of ocean heat content from 1960 to 2015. *Sci. Adv.*, 3, e1601545,
1353 <https://doi.org/10.1126/sciadv.1601545>, 2017.

1354 Cheng, L., Trenberth, K. E., Fasullo, J. T., Mayer, M., Balmaseda, M., and Zhu, J.:
1355 Evolution of Ocean Heat Content Related to ENSO. *J. Climate*, 32, 3529-3556,
1356 <https://doi.org/10.1175/jcli-d-18-0607.1>, 2019.

1357 Cheng, L., Trenberth, K. E., Gruber, N., Abraham, J. P., Fasullo, J. T., Li, G., Mann, M. E.,
1358 Zhao, X., and Zhu, J.: Improved Estimates of Changes in Upper Ocean Salinity and
1359 the Hydrological Cycle. *J. Climate*, 33, 10357-10381, <https://doi.org/10.1175/JCLI->
1360 [D-20-0366.1](https://doi.org/10.1175/JCLI-D-20-0366.1), 2020.

1361 Cheng, L., von Schuckmann, K., Abraham, J. P., Trenberth, K. E., Mann, M. E., Zanna, L.,
1362 England, M. H., Zika, J. D., Fasullo, J. T., Yu, Y., Pan, Y., Zhu, J., Newsom, E. R.,
1363 Bronselaer, B., and Lin, X.: Past and future ocean warming. *Nat. Rev. Earth Env.*, 3,
1364 776-794, <https://doi.org/10.1038/s43017-022-00345-1>, 2022a.

1365 Cheng, L., Foster, G., Hausfather, Z., Trenberth, K. E., and Abraham, J.: Improved
1366 quantification of the rate of ocean warming. *J. Climate*, 35, 4827-4840,
1367 <https://doi.org/10.1175/jcli-d-20-0366.1>, 2022b.

1368 Cheng, L., Tan, Z., Pan, Y., Zheng, H., Zhu, Y., Wei, W., Du, J., Li, G., Ye, H., Gourteski,
1369 V.: IAP temperature 1° gridded analysis product (IAPv4),
1370 <http://dx.doi.org/10.12157/IOCAS.20240117.002>, 2024a.

1371 Cheng, L., Tan, Z., Pan, Y., Zheng, H., Zhu, Y., Wei, W., Du, J., Li, G., Ye, H., Gourteski,
1372 V.: IAP global ocean heat content 1° gridded analysis product (IAPv4),
1373 <http://dx.doi.org/10.12157/IOCAS.20240117.001>, 2024b.

1374 Chu, P. C., and Fan, C.: Global climatological data of ocean thermohaline parameters
1375 derived from WOA18. *Scientific Data*, 10, 408, <https://doi.org/10.1038/s41597-023->
1376 [02308-7](https://doi.org/10.1038/s41597-023-02308-7), 2023.

1377 Comiso, J. C., Meier, W. N., and Gersten, R.: Variability and trends in the Arctic Sea ice
1378 cover: Results from different techniques. *J. Geophys. Res.- Oceans*, 122, 6883-6900,
1379 <https://doi.org/10.1002/2017JC012768>, 2017.

1380 Cowley, R., Killick, R. E., Boyer, T., Gouretski, V., Reseghetti, F., Kizu, S., Palmer, M.
1381 D., Cheng, L., Storto, A., Le Menn, M., Simoncelli, S., Macdonald, A. M., &
1382 Domingues, C. M.: International Quality-Controlled Ocean Database (iQuOD) v0.1:
1383 The Temperature Uncertainty Specification. *Front. Mar. Sci.*, 8,
1384 <https://doi.org/10.3389/fmars.2021.689695>, 2021.

1385 Dangendorf, S., Frederikse, T., Chafik, L., Klinck, J. M., Ezer, T., and Hamlington, B. D.:
1386 Data-driven reconstruction reveals large-scale ocean circulation control on coastal
1387 sea level. *Nat. Clim. Change*, 11, 514-520, [https://doi.org/10.1038/s41558-021-](https://doi.org/10.1038/s41558-021-01046-1)
1388 01046-1, 2021.

1389 de Boyer Montégut, C., Madec, G., Fischer, A. S., Lazar, A., and Iudicone, D.: Mixed
1390 layer depth over the global ocean: An examination of profile data and a profile-based
1391 climatology. *J. Geophys. Res.- Oceans*, 109, <https://doi.org/10.1029/2004JC002378>,
1392 2004.

1393 [Desbruyères, D., McDonagh, E. L., King, B. A. & Thierry, V. Global and full-depth ocean](#)
1394 [temperature trends during the early twenty-first century from Argo and repeat](#)
1395 [hydrography. *J. Clim.* 30, 1985–1997, 2017.](#)

1396 England, M. H., McGregor, S., Spence, P., Meehl, G. A., Timmermann, A., Cai, W.,
1397 Gupta, A. S., McPhaden, M. J., Purich, A., & Santoso, A.: Recent intensification of
1398 wind-driven circulation in the Pacific and the ongoing warming hiatus. *Nat. Clim.*
1399 *Change*, 4, 222-227, <https://doi.org/10.1038/nclimate2106>, 2014.

1400 Fasullo, J. T., and Nerem, R. S.: Altimeter-era emergence of the patterns of forced sea-
1401 level rise in climate models and implications for the future. *P. Natl. Acad. Sci.*, 115,
1402 12944-12949, <https://doi.org/10.1073/pnas.1813233115>, 2018.

1403 Frederikse, T., Landerer, F., Caron, L., Adhikari, S., Parkes, D., Humphrey, V. W.,
1404 Dangendorf, S., Hogarth, P., Zanna, L., Cheng, L., and Wu, Y.-H.: The causes of sea
1405 level rise since 1900. *Nature*, 584, 393-397, [https://doi.org/10.1038/s41586-020-](https://doi.org/10.1038/s41586-020-2591-3)
1406 2591-3, 2020.

1407 Garcia, H. E., Boyer, T. P., Locarnini, R. A., Baranova, O. K., and Zweng, M. M.: *World*
1408 *Ocean Database 2018: User's Manual.*, T. E. A.V. Mishonov, NOAA, Silver Spring,
1409 MD., Ed. , 2018

1410 Goni, G. J., Sprintall, J., Bringas, F., Cheng, L., Cirano, M., Dong, S., Domingues, R.,
1411 Goes, M., Lopez, H., Morrow, R., Rivero, U., Rossby, T., Todd, R. E., Trinanés, J.,
1412 Zilberman, N., Baringer, M., Boyer, T., Cowley, R., Domingues, Hutchinson, K.,
1413 Kramp, M., Mata, M. M., Reseghetti, F., Sun, C., Bhaskar Tvs U., Volkov, D.: More
1414 Than 50 Years of Successful Continuous Temperature Section Measurements by the
1415 Global Expendable Bathythermograph Network, Its Integrability, Societal Benefits,
1416 and Future. *Fron. Mar. Sci.*, 6, <http://dx.doi.org/10.3389/fmars.2019.00452>, 2019.

1417 Good, S. A., Martin, M. J., and Rayner, N. A.: EN4: Quality controlled ocean temperature
1418 and salinity profiles and monthly objective analyses with uncertainty estimates. *J.*
1419 *Geophys. Res. Oceans*, 118, 6704-6716, <https://doi.org/10.1002/2013jc009067>, 2013.
1420 Gouretski, V., and Koltermann, K. P.: How much is the ocean really warming? *Geophys.*
1421 *Res. Lett.*, 34, L01610, <https://doi.org/10.1029/2006GL027834>, 2007.
1422 Gouretski, V. and Reseghetti, F.: On depth and temperature biases in bathythermograph
1423 data: Development of a new correction scheme based on analysis of a global ocean
1424 database, *Deep Sea Res.*, 57, 6, 812-833, <https://doi.org/10.1016/j.dsr.2010.03.011>,
1425 2010.
1426 Gouretski, V., and Cheng, L.: Correction for Systematic Errors in the Global Dataset of
1427 Temperature Profiles from Mechanical Bathythermographs. *J. Atmos. Ocean.*
1428 *Technol.*, 37, 841-855, <https://doi.org/10.1175/jtech-d-19-0205.1>, 2020.
1429 Gouretski, V., Cheng, L., and Boyer, T.: On the Consistency of the Bottle and CTD Profile
1430 Data. *J. Atmos. Ocean Technol.*, 39, 1869-1887, [https://doi.org/10.1175/JTECH-D-](https://doi.org/10.1175/JTECH-D-22-0004.1)
1431 [22-0004.1](https://doi.org/10.1175/JTECH-D-22-0004.1), 2022.
1432 Gouretski, V., Roquet, F., and Cheng, L.: Measurement biases in ocean temperature
1433 profiles from marine mammal data loggers. *J. Atmos. Ocean Technol.*, submitted,
1434 2024.
1435 Gouretski, V., Kennedy, J., Boyer, T., and Köhl, A.: Consistent near-surface ocean
1436 warming since 1900 in two largely independent observing networks. *Geophys. Res.*
1437 *Lett.*, 39, <https://doi.org/10.1029/2012GL052975>, 2012.
1438 [Gouretski V, Koltermann K P. 2004. WOCE global hydrographic clima- tology. *Berichte*](#)
1439 [des BSH, 35: 1–52.](#)
1440 Gulev, S. K., Thorne, P. W., Ahn, J., Dentener, F. J., Domingues, C. M., Gerland, S.,
1441 Gong, D., Kaufman, D. S., Nnamchi, H. C., Quaas, J., Rivera, J. A., Sathyendranath,
1442 S., Smith, S. L., Trewin, B., Schuckmann, K. von, and Vose, R. S.: Changing State
1443 of the Climate System Supplementary Material, in: *Climate Change 2021: The*
1444 *Physical Science Basis. Contribution of Working Group I to the Sixth Assessment*
1445 *Report of the Intergovernmental Panel on Climate Change*, edited by: Masson-
1446 Delmotte, V., Zhai, P., Pirani, A., Connors, S. L., Péan, C., Berger, S., Caud, N.,
1447 Chen, Y., Goldfarb, L., Gomis, M. I., Huang, M., Leitzell, K., Lonnoy, E., Matthews,
1448 J. B. R., Maycock, T. K., Waterfield, T., Yelekçi, O., Yu, R., and Zhou, B.,
1449 Cambridge University Press, Cambridge, United Kingdom and New York, NY,
1450 USA, 287–422, <https://doi.org/10.1017/9781009157896.004>, 2021.

1451 Hakuba, M. Z., Frederikse, T., and Landerer, F. W.: Earth's Energy Imbalance From the
1452 Ocean Perspective (2005–2019), *Geophys. Res. Lett.*, 48, e2021GL093624,
1453 <https://doi.org/10.1029/2021GL093624>, 2021.

1454 Hansen, J., Sato, M., Kharecha, P., and von Schuckmann, K.: Earth's energy imbalance and
1455 implications. *Atmos. Chem. Phys.*, 11, 13421-13449, [https://doi.org/10.5194/acp-11-](https://doi.org/10.5194/acp-11-13421-2011)
1456 [13421-2011](https://doi.org/10.5194/acp-11-13421-2011), 2011.

1457 Hirahara, S., Ishii, M., and Fukuda, Y.: Centennial-Scale Sea Surface Temperature
1458 Analysis and Its Uncertainty. *J. Climate*, 27, 57-75, [https://doi.org/10.1175/JCLI-D-](https://doi.org/10.1175/JCLI-D-12-00837.1)
1459 [12-00837.1](https://doi.org/10.1175/JCLI-D-12-00837.1), 2014.

1460 Holte, J., Talley, L. D., Gilson, J., and Roemmich, D.: An Argo mixed layer climatology
1461 and database. *Geophys. Res. Lett.*, 44, 5618-5626,
1462 <https://doi.org/10.1002/2017GL073426>, 2017.

1463 Hosoda, S., Ohira, T., and Nakamura, T.: Monthly mean dataset of global oceanic
1464 temperature and salinity derived from Argo float observations. JAMSTEC Report of
1465 Research and Development, 8, <https://doi.org/10.5918/jamstecr.8.47>, 2008.

1466 Huang, B., Thorne, P. W., Banzon, V. F., Boyer, T., Chepurin, G., Lawrimore, J. H.,
1467 Menne, M. J., Smith, T. M., Vose, R. S., and Zhang, H.-M.: Extended Reconstructed
1468 Sea Surface Temperature, Version 5 (ERSSTv5): Upgrades, Validations, and
1469 Intercomparisons. *J. Climate*, 30, 8179-8205, [https://doi.org/10.1175/JCLI-D-16-](https://doi.org/10.1175/JCLI-D-16-0836.1)
1470 [0836.1](https://doi.org/10.1175/JCLI-D-16-0836.1), 2017.

1471 Hugonnet, R., McNabb, R., Berthier, E., Menounos, B., Nuth, C., Girod, L., Farinotti, D.,
1472 Huss, M., Dussailant, I., Brun, F., and Kääb, A.: Accelerated global glacier mass
1473 loss in the early twenty-first century. *Nature*, 592, 726-731,
1474 <https://doi.org/10.1038/s41586-021-03436-z>, 2021.

1475 IPCC: Annex I: Observational Products [Trewin, B. (ed.)], pp. 2061–2086 pp. , 2021

1476 Ishii, M., and Kimoto, M.: Reevaluation of historical ocean heat content variations with
1477 time-varying XBT and MBT depth bias corrections. *J. Oceanogr.*, 65, 287-299,
1478 <https://doi.org/10.1007/s10872-009-0027-7>, 2009.

1479 Ishii, M., Shouji, A., Sugimoto, S., and Matsumoto, T.: Objective analyses of sea-surface
1480 temperature and marine meteorological variables for the 2⁰th century using ICOADS
1481 and the Kobe Collection. *Int. J. Climatol.*, 25, 865-879,
1482 <https://doi.org/10.1002/joc.1169>, 2005.

1483 Ishii, M., Y. Fukuda, S. Hirahara, S. Yasui, T. Suzuki, and K. Sato: Accuracy of Global
1484 Upper Ocean Heat Content Estimation Expected from Present Observational Data
1485 Sets. *Sola*, 13, 163-167, <https://doi.org/10.2151/sola.2017-030>, 2017.

1486 Jin, F.-F.: An Equatorial Ocean Recharge Paradigm for ENSO. Part I: Conceptual Model.
1487 *J. Atmos. Sci.*, 54, 811-829, [https://doi.org/10.1175/1520-0469\(1997\)054%3C0811:AEORPF%3E2.0.CO;2](https://doi.org/10.1175/1520-0469(1997)054%3C0811:AEORPF%3E2.0.CO;2), 1997.

1489 [Jin, Y., Li, Y., Cheng, L., Duan, J., Li, R., & Wang, F.. Ocean heat content increase of the
1490 Maritime Continent since the 1990s. *Geophysical Research Letters*, 51,
1491 e2023GL107526. <https://doi.org/10.1029/2023GL107526>, 2024.](https://doi.org/10.1029/2023GL107526)

1492 Johns, W. E., Elipot, S., Smeed, D. A., Moat, B., King, B., Volkov, D. L., and Smith, R. H.:
1493 Towards two decades of Atlantic Ocean mass and heat transports at 26.5° N.
1494 *Philosophical Transactions of the Royal Society A: Mathematical, Physical and
1495 Engineering Sciences*, 381, 20220188, 2023.

1496 Johnson, G. C., Purkey, S. G., Zilberman, N. V., and Roemmich, D.: Deep Argo Quantifies
1497 Bottom Water Warming Rates in the Southwest Pacific Basin. *Geophys. Res. Lett.*,
1498 46, 2662-2669, <https://doi.org/10.1098/rsta.2022.0188>, 2019.

1499 Katsumata, K., Purkey, S. G., Cowley, R., Sloyan, B. M., Diggs, S. C., Moore, T. S.,
1500 Talley, L. D., and Swift, J. H.: GO-SHIP Easy Ocean: Gridded ship-based
1501 hydrographic section of temperature, salinity, and dissolved oxygen. *Scientific Data*,
1502 9, 103, <https://doi.org/10.1038/s41597-022-01212-w>, 2022.

1503 Kennedy, J.: A review of uncertainty in in situ measurements and data sets of sea surface
1504 temperature. *Rev. Geophys.*, 52, 1-32, <https://doi.org/10.1002/2013RG000434>, 2014.

1505 Levitus, S., Antonov, J. I., Boyer, T. P., Locarnini, R. A., Garcia, H. E., and Mishonov, A.
1506 V.: Global ocean heat content 1955–2008 in light of recently revealed
1507 instrumentation problems. *Geophys. Res. Lett.*, 36,
1508 <https://doi.org/10.1029/2008GL037155>, 2009

1509 Levitus, S., Antonov, J. I., Boyer, T. P., Baranova, O. K., Garcia, H. E., Locarnini, R. A.,
1510 Mishonov, A. V., Reagan, J. R., Seidov, D., Yarosh, E. S., and Zweng, M. M.: World
1511 ocean heat content and thermocline sea level change (0–2000 m), 1955–2010,
1512 *Geophys. Res. Lett.*, 39, L10603, <https://doi.org/10.1029/2012GL051106>, 2012.

1513 Li, G., Cheng, L., Zhu, J., Trenberth, K. E., Mann, M. E., and Abraham, J. P.: Increasing
1514 ocean stratification over the past half-century. *Nat. Clim. Change*, 10, 1116-1123,
1515 <https://doi.org/10.1038/s41558-020-00918-2>, 2020.

1516 Li, H., Xu, F., Zhou, W., Wang, D., Wright, J. S., Liu, Z., and Lin, Y.: Development of a
1517 global gridded Argo data set with Barnes successive corrections. *J. Geophys. Res.*
1518 *Oceans*, 122, 866-889, <https://doi.org/10.1002/2016JC012285>, 2017.

1519 Li, Y., Church, J. A., McDougall, T. J., and Barker, P. M.: Sensitivity of Observationally
1520 Based Estimates of Ocean Heat Content and Thermal Expansion to Vertical
1521 Interpolation Schemes. *Geophys. Res. Lett.*, 49, e2022GL101079,
1522 <https://doi.org/10.1029/2022GL101079>, 2022.

1523 Lian, T., Wang, J., Chen, D., Liu, T. and Wang, D.: A Strong 2023/24 El Niño is Staged by
1524 Tropical Pacific Ocean Heat Content Buildup. *Ocean-Land-Atmosphere Research*, 2,
1525 0011, <https://doi.org/10.34133/olar.0011>, 2023.

1526 Liu, C., and Allan, R.: Reconstructions of the radiation fluxes at the top of atmosphere and
1527 net surface energy flux: DEEP-C version 5.0. . a. A. University of Reading Dataset,
1528 Ed., <https://doi.org/10.17864/1947.000347>, 2022

1529 Liu, C., Allan, R. P., Mayer, M., Hyder, P., Loeb, N. G., Roberts, C. D., Valdivieso, M.,
1530 Edwards, J. M., and Vidale, P.-L.: Evaluation of satellite and reanalysis-based global
1531 net surface energy flux and uncertainty estimates. *J. Geophys. Res.- Atmospheres*,
1532 122, 6250-6272, <https://doi.org/10.1002/2017JD026616>, 2017.

1533 Liu, C., Allan, R. P., Mayer, M., Hyder, P., Desbruyères, D., Cheng, L., Xu, J., Xu, F., and
1534 Zhang, Y.: Variability in the global energy budget and transports 1985–2017, *Clim.*
1535 *Dynam.*, 55, 3381– 3396, <https://doi.org/10.1007/s00382-020-05451-8>, 2020.

1536 [Loeb, N. G., B. A. Wielicki, D. R. Doelling, G. L. Smith, D. F. Keyes, S. Kato, N. Manalo-](#)
1537 [Smith, and T. Wong: Toward Optimal Closure of the Earth's Top-of-Atmosphere](#)
1538 [Radiation Budget. *J. Climate*, 22, 748–766. <https://doi.org/10.1175/2008JCLI2637.1>,](#)
1539 [2009.](#)

1540 Loeb, N. G., Johnson, G. C., Thorsen, T. J., Lyman, J. M., Rose, F. G., and Kato, S.:
1541 Satellite and Ocean Data Reveal Marked Increase in Earth's Heating Rate. *Geophys.*
1542 *Res. Lett.*, 48, <https://doi.org/10.1029/2021gl093047>, 2021.

1543 Loeb, N. G., Thorsen, T. J., Norris, J. R., Wang, H., and Su, W.: Changes in Earth's energy
1544 budget during and after the “Pause” in global warming: An observational
1545 perspective, *Climate*, 6, 62, <https://doi.org/10.3390/cli6030062>, 2018.

1546 Lyman, J. M., and Johnson, G. C.: Estimating Global Ocean Heat Content Changes in the
1547 Upper 1800 m since 1950 and the Influence of Climatology Choice. *J. Climate*, 27,
1548 1945-1957, <https://doi.org/10.1175/JCLI-D-12-00752.1>, 2014.

1549 Lyman, J. M., Good, S. A., Gouretski, V. V., Ishii, M., Johnson, G. C., Palmer, M. D.,
1550 Smith, D. M., and Willis, J. K.: Robust warming of the global upper ocean. *Nature*,
1551 465, 334-337, <https://doi.org/10.1038/nature09043>, 2010.

1552 [Lyman, J. M., and G. C. Johnson, 2023: Global High-Resolution Random Forest](#)
1553 [Regression Maps of Ocean Heat Content Anomalies Using In Situ and Satellite Data.](#)
1554 [J. Atmos. Oceanic Technol., 40, 575–586, \[https://doi.org/10.1175/JTECH-D-22-\]\(https://doi.org/10.1175/JTECH-D-22-0058.1\)](#)
1555 [0058.1.](#)

1556 Mann, M.E., Beyond the Hockey Stick: Climate Lessons from The Common Era, *Proc.*
1557 *Natl. Acad. Sci.*, 118 (39) e2112797118, <https://doi.org/10.1073/pnas.2112797118>,
1558 2021.

1559 [McDougall T. J. and P. M. Barker, 2011: Getting started with TEOS-10 and the Gibbs](#)
1560 [Seawater \(GSW\) Oceanographic Toolbox, 28pp., SCOR/IAPSO WG127, ISBN 978-](#)
1561 [0-646-55621-5.](#)

1562 Mayer, J., Mayer, M., and Haimberger, L.: Consistency and Homogeneity of Atmospheric
1563 Energy, Moisture, and Mass Budgets in ERA5. *J. Climate*, 34, 3955-3974,
1564 <https://doi.org/10.1175/JCLI-D-20-0676.1>, 2021.

1565 Mayer, M., Alonso Balmaseda, M., and Haimberger, L.: Unprecedented 2015/2016 Indo-
1566 Pacific Heat Transfer Speeds Up Tropical Pacific Heat Recharge. *Geophys. Res.*
1567 *Let.*, 45, 3274-3284, <https://doi.org/10.1002/2018GL077106>, 2018.

1568 McPhaden, M. J.: A 2^{1st} century shift in the relationship between enso sst and warm water
1569 volume anomalies. *Geophys. Res. Let.*, 39, 9706,
1570 <https://doi.org/10.1029/2012GL051826>, 2012.

1571 McMahon, C. R., Roquet, F., Baudel, S., Belbeoch, M., Bestley, S., Blight, C., Boehme,
1572 L., Carse, F., Costa, D. P., Fedak, M. A., Guinet, C., Harcourt, R., Heslop, E.,
1573 Hindell, M. A., Hoenner, X., Holland, K., Holland, M., Jaine, F. R. A., Jeanniard du
1574 Dot, T., . . . Woodward: Animal Borne Ocean Sensors – AniBOS – An Essential
1575 Component of the Global Ocean Observing System. *Front. Mar. Sci.*, 8,
1576 <https://doi.org/10.3389/fmars.2021.751840>, 2021.

1577 Meyssignac, B., Boyer, T., Zhao, Z., Hakuba, M. Z., Landerer, F. W., Stammer, D., Köhl,
1578 A., Kato, S., L’Ecuyer, T., Ablain, M., Abraham, J. P., Blazquez, A., Cazenave, A.,
1579 Church, J. A., Cowley, R., Cheng, L., Domingues, C. M., Giglio, D., Gouretski, V.,
1580 Ishii, M., Johnson, G. C., Killick, R. E., Legler, D., Llovel, W., Lyman, J., Palmer,
1581 M. D., Piotrowicz, S., Purkey, S. G., Roemmich, D., Roca, R., Savita, A.,
1582 Schuckmann, K. von, Speich, S., Stephens, G., Wang, G., Wijffels, S. E., and

1583 Zilberman, N.: Measuring Global Ocean Heat Content to Es-
1584 timate the Earth Energy Imbalance. *Front. Mar. Sci.*, 6, 432, <https://doi.org/10.3389/fmars.2019.00432>, 2019.

1585 Minière, A., von Schuckmann, K., Sallée, J.-B., and Vogt, L.: Robust acceleration of Earth
1586 system heating observed over the past six decades. *Sci. Rep.*, 13, 22975,
1587 <https://doi.org/10.1038/s41598-023-49353-1>, 2024

1588 Nerem, R. S., Beckley, B. D., Fasullo, J. T., Hamlington, B. D., Masters, D., and Mitchum,
1589 G. T.: Climate-change-driven accelerated sea-level rise detected in the altimeter era.
1590 *P. Natl. Acad. Sci.*, 115, 2022-2025, <https://doi.org/10.1073/pnas.1717312115>, 2018.

1591 O'Carroll, A. G., Armstrong, E. M., Beggs, H. M., Bouali, M., Casey, K. S., Corlett, G. K.,
1592 Dash, P., Donlon, C. J., Gentemann, C. L., Høyer, J. L., Ignatov, A., Kabobah, K.,
1593 Kachi, M., Kurihara, Y., Karagali, I., Maturi, E., Merchant, C. J., Marullo, S.,
1594 Minnett, P. J., Pennybacker, M., Ramakrishnan, B., Ramsankaran, R. Santoleri, R.,
1595 Sunder, S., Saux Picart, S. Vázquez-Cuervo, J., Wimmer, W.: Observational Needs
1596 of Sea Surface Temperature. *Front. Mar. Sci.*, 6,
1597 <https://doi.org/10.3389/fmars.2019.00420>, 2019.

1598 Oliver, E. C. J., Benthuisen, J.A., Darmaraki, S., Donat, M. G., Hobday, A. J., Holbrook,
1599 N. J., Schlegel, R.W., and Sen Gupta A., Marine Heatwaves. *Annual review of*
1600 *marine science* 13, 313-342, [https://doi.org/10.1146/annurev-marine-032720-](https://doi.org/10.1146/annurev-marine-032720-095144)
1601 [095144](https://doi.org/10.1146/annurev-marine-032720-095144), 2021.

1602 Purkey, S. G., and Johnson, G. C.: Warming of Global Abyssal and Deep Southern Ocean
1603 Waters between the 1990s and 2000s: Contributions to Global Heat and Sea Level
1604 Rise Budgets. *J. Climate*, 23, 6336-6351, <https://doi.org/10.1175/2010jcli3682.1>,
1605 2010.

1606 Palmer, M. D., and K. Haines: Estimating Oceanic Heat Content Change Using Isotherms.
1607 *J. Climate*, 22, 4953-4969, <https://doi.org/10.1175/2009JCLI2823.1>, 2009.

1608 Rahmstorf, S., Box, J., Feulner, G., Mann, M.E., Robinson, A., Rutherford, S.,
1609 Schaffernicht, E. Exceptional 2⁰h-Century slowdown in Atlantic Ocean
1610 overturning, *Nature Climate Change*, 5, 475-480, 2015.

1611 Rayner, N. A., Parker, D. E., Horton, E. B., Folland, C. K., Alexander, L. V., Rowell, D.
1612 P., Kent, E. C., and Kaplan, A.: Global analyses of sea surface temperature, sea ice,
1613 and night marine air temperature since the late nineteenth century. *J. Geophys. Res.-*
1614 *Atmospheres*, 108, <https://doi.org/https://doi.org/10.1029/2002JD002670>, 2003.

- 设置了格式: 字体: 非倾斜
- 设置了格式: 字体: 非倾斜
- 设置了格式: 字体: 非倾斜
- 设置了格式: 字体: 非倾斜, (中文) 中文(中国)
- 设置了格式: 字体: 非倾斜
- 设置了格式: 字体: 非倾斜

1615 Reiniger, R. F., and Ross, C. K.: A method of interpolation with application to
1616 oceanographic data. *Deep Sea Research*, 15, 185-193, [https://doi.org/10.1016/0011-](https://doi.org/10.1016/0011-7471(68)90040-5)
1617 [7471\(68\)90040-5](https://doi.org/10.1016/0011-7471(68)90040-5), 1968.

1618 [Rhein, M., S.R. Rintoul, S. Aoki, E. Campos, D. Chambers, R.A. Feely, S. Gulev, G.C.](#)
1619 [Johnson, S.A. Josey, A. Kostianoy, C. Mauritzen, D. Roemmich, L.D. Talley and F.](#)
1620 [Wang, 2013: Observations: Ocean. In: Climate Change 2013: The Physical Science](#)
1621 [Basis. Contribution of Working Group I to the Fifth Assessment Report of the](#)
1622 [Intergovernmental Panel on Climate Change \[Stocker, T.F., D. Qin, G.-K. Plattner,](#)
1623 [M. Tignor, S.K. Allen, J. Boschung, A. Nauels, Y. Xia, V. Bex and P.M. Midgley](#)
1624 [\(eds.\)\]. Cambridge University Press, Cambridge, United Kingdom and New York,](#)
1625 [NY, USA.](#)

1626 Roemmich, D., and Gilson, J.: The 2004–2008 mean and annual cycle of temperature,
1627 salinity, and steric height in the global ocean from the Argo Program. *Prog.*
1628 *Oceanogr.*, 82, 81-100, <https://doi.org/10.1016/j.pocean.2009.03.004>, 2009.

1629 Roemmich, D., and Gilson, J.: The global ocean imprint of ENSO. *Geophys. Res. Lett.*, 38,
1630 <https://doi.org/10.1029/2011GL047992>, 2011.

1631 Roemmich, D., Alford, M. H., Claustre, H., Johnson, K., King, B., Moum, J., Oke, P.,
1632 Owens, W. B., Pouliquen, S., Purkey, S., Scanderbeg, M., Suga, T., Wijffels, S.,
1633 Zilberman, N., Bakker, D., Baringer, M., Belbeoch, M., Bittig, H. C., Boss, E., . . .
1634 Yasuda, I.: On the Future of Argo: A Global, Full-Depth, Multi-Disciplinary Array.
1635 *Front. Mar. Sci.*, 6, 2019.

1636 [Savita, A., and Coauthors: Quantifying Spread in Spatiotemporal Changes of Upper-Ocean](#)
1637 [Heat Content Estimates: An Internationally Coordinated Comparison. *J. Climate*, 35,](#)
1638 [851–875, <https://doi.org/10.1175/JCLI-D-20-0603.1>, 2022.](#)

1639 Sloyan, B. M., Wanninkhof, R., Kramp, M., Johnson, G. C., Talley, L. D., Tanhua, T.,
1640 McDonagh, E., Cusack, C., O'Rourke, E., McGovern, E., Katsumata, K., Diggs, S.,
1641 Hummon, J., Ishii, M., Azetsu-Scott, K., Boss, E., Ansorge, I., Perez, F. F., Mercier,
1642 H., . . . Campos, E.: The Global Ocean Ship-Based Hydrographic Investigations
1643 Program (GO-SHIP): A Platform for Integrated Multidisciplinary Ocean Science.
1644 *Front. Mar. Sci.*, 6, 2019.

1645 [Sun, D., Li, F., Jing, Z. et al. Frequent marine heatwaves hidden below the surface of the](#)
1646 [global ocean. *Nat. Geosci.* 16, 1099–1104, \[https://doi.org/10.1038/s41561-023-\]\(https://doi.org/10.1038/s41561-023-01325-w\)](#)
1647 [01325-w](https://doi.org/10.1038/s41561-023-01325-w), 2023.

1648 [Su, H. et al. OPEN: a new estimation of global ocean heat content for upper 2000 meters](#)
1649 [from remote sensing data. *Remote Sens.* <https://doi.org/10.3390/rs12142294>, 2020.](#)

1650 Tan, Z., Zhang, B., Wu, X., Dong, M., and Cheng, L.: Quality control for ocean
1651 observations: From present to future. *Science China Earth Sciences*, 65, 215-233,
1652 <https://doi.org/10.1007/s11430-021-9846-7>, 2022.

1653 Tan, Z., Cheng, L., Gouretski, V., Zhang, B., Wang, Y., Li, F., Liu, Z., & Zhu, J.: A new
1654 automatic quality control system for ocean profile observations and impact on ocean
1655 warming estimate. *Deep Sea Research Part I: Oceanographic Research Papers*, 194,
1656 103961, <https://doi.org/10.1016/j.dsr.2022.103961>, 2023.

1657 Trenberth, K. E.: *The Changing Flow of Energy Through the Climate System*.
1658 Cambridge University Press., <https://doi.org/10.1017/9781108979030>, 2022.

1659 Trenberth, K. E., and Fasullo, J. T.: Atlantic meridional heat transports computed from
1660 balancing Earth's energy locally. *Geophys. Res. Lett.*, 44, 1919-1927,
1661 <https://doi.org/10.1002/2016gl072475>, 2017.

1662 Trenberth, K. E., Fasullo, J. T., and Kiehl, J.: Earth's Global Energy Budget *Bull. Am.*
1663 *Meteorol. Soc.*, 90, 311-324, <https://doi.org/10.1175/2008bams2634.1>, 2009.

1664 Trenberth, K. E., Fasullo, J. T., Von Schuckmann, K., and Cheng, L.: Insights into Earth's
1665 Energy Imbalance from Multiple Sources. *J. Climate*, 29, 7495-7505,
1666 <https://doi.org/10.1175/jcli-d-16-0339.1>, 2016.

1667 Trenberth, K. E., Zhang, Y., Fasullo, J. T., and Cheng, L.: Observation-Based Estimates of
1668 Global and Basin Ocean Meridional Heat Transport Time Series. *J. Climate*, 32,
1669 4567-4583, <https://doi.org/10.1175/jcli-d-18-0872.1>, 2019.

1670 von Schuckmann, K., and Le Traon, P. Y.: How well can we derive Global Ocean
1671 Indicators from Argo data? *Ocean Sci.*, 7, 783-791, [https://doi.org/10.5194/os-7-783-](https://doi.org/10.5194/os-7-783-2011)
1672 2011, 2011.

1673 von Schuckmann, K., Cheng, L., Palmer, M. D., Hansen, J., Tassone, C., Aich, V.,
1674 Adusumilli, S., Beltrami, H., Boyer, T., Cuesta-Valero, F. J., Desbruyères, D.,
1675 Domingues, C., García-García, A., Gentine, P., Gilson, J., Gorfer, M., Haim-berger,
1676 L., Ishii, M., Johnson, G. C., Killick, R., King, B. A., Kirchengast, G.,
1677 Kolodziejczyk, N., Lyman, J., Marzeion, B., Mayer, M., Monier, M., Monselesan, D.
1678 P., Purkey, S., Roemmich, D., Schweiger, A., Seneviratne, S. I., Shepherd, A., Slater,
1679 D. A., Steiner, A. K., Straneo, F., Timmermans, M.-L., and Wijffels, S. E.: Heat
1680 stored in the Earth system: where does the energy go?, *Earth Syst. Sci. Data*, 12,
1681 2013–2041, <https://doi.org/10.5194/essd-12-2013-2020>, 2020.

设置了格式: 字体: 倾斜

1682 von Schuckmann, K., Palmer, M. D., Trenberth, K. E., Cazenave, A., Chambers, D.,
1683 Champollion, N., Hansen, J., Josey, S. A., Loeb, N., Mathieu, P.-P., Meyssignac, B.,
1684 and Wild, M.: An imperative to monitor Earth's energy imbalance, *Nat. Clim.*
1685 *Change*, 6, 138–144, <https://doi.org/10.1038/nclimate2876>, 2016.

1686 von Schuckmann, K. Minière, A. Gues, F. Cuesta-Valero, F. J. Kirchengast, G.
1687 Adusumilli, S. Straneo, F. Ablain, M. Allan, R. P. Barker, P. M. Beltrami, H.
1688 Blazquez, A. Boyer, T. Cheng, L. Church, J. Desbruyeres, D. Dolman, H.
1689 Domingues, C. M. García-García, A. Giglio, D. Gilson, J. E. Gorfer, M. Haimberger,
1690 L. Hakuba, M. Z. Hendricks, S. Hosoda, S. Johnson, G. C. Killick, R. King, B.
1691 Kolodziejczyk, N. Korosov, A. Krinner, G. Kuusela, M. Landerer, F. W. Langer, M.
1692 Lavergne, T. Lawrence, I. Li, Y. Lyman, J. Marti, F. Marzeion, B. Mayer, M.
1693 MacDougall, A. H. McDougall, T. Monselesan, D. P. Nitzbon, J. Ootosaka, I. Peng, J.
1694 Purkey, S. Roemmich, D. Sato, K. Sato, K. Savita, A. Schweiger, A. Shepherd, A.
1695 Seneviratne, S. I. Simons, L. Slater, D. A. Slater, T. Steiner, A. K. Suga, T. Szekely,
1696 T. Thiery, W. Timmermans, M. L. Vanderkelen, I. Wjiffels, S. E. Wu, T. Zemp, M.:
1697 Heat stored in the Earth system 1960–2020: where does the energy go? *Earth Syst.*
1698 *Sci. Data*, 15, 1675-1709, <https://doi.org/10.5194/essd-15-1675-2023>, 2023.

1699 Wang, F., Shen, Y., Chen, Q., and Sun, Y.: Reduced misclosure of global sea-level budget
1700 with updated Tongji-Grace2018 solution. *Sci Rep-Uk*, 11, 17667,
1701 <https://doi.org/10.1038/s41598-021-96880-w>, 2021.

1702 Watkins, M. M., Wiese, D. N., Yuan, D. N., Boening, C., and Landerer, F. W.: Improved
1703 methods for observing Earth's time variable mass distribution with GRACE using
1704 spherical cap mascons. *J. Geophys. Res.- Solid Earth*, 120, 2648-2671,
1705 <https://doi.org/10.1002/2014JB011547>, 2015.

1706 Wjiffels, S. E., Willis, J., Domingues, C. M., Barker, P., White, N. J., Gronell, A.,
1707 Ridgway, K., and Church, J. A.: Changing Expendable Bathythermograph Fall Rates
1708 and Their Impact on Estimates of Thermosteric Sea Level Rise. *J. Climate*, 21, 5657-
1709 5672, <https://doi.org/10.1175/2008jcli2290.1>, 2008.

1710 WMO: State of the Global Climate 2021, WMO-No. 1290, 2022.

1711 Wong, A. P. S., Wjiffels, S. E., Riser, S. C., et al.: Argo Data 1999–2019: Two Million
1712 Temperature-Salinity Profiles and Subsurface Velocity Observations From a Global
1713 Array of Profiling Floats, <https://doi.org/10.3389/fmars.2020.00700>, 2020.

1714 [Zanna, L., Khatiwala, S., Gregory, J. M., Ison, J. & Heimbach, P. Global reconstruction of](#)
1715 [historical ocean heat storage and transport. *Proc. Natl Acad. Sci. USA* 116, 1126–](#)
1716 [1131, <https://doi.org/10.1073/pnas.1808838115>, 2019.](#)
1717 [Zhang, B. et al. CAS-Ocean Data Center, Global Ocean Science Database \(CODCv1\):](#)
1718 [temperature. Marine Science Data Center of the Chinese Academy of Science, _](#)
1719 [doi:10.12157/IOCAS.20230525.001 \(2024\).](#)
1720 Zhang, X., Church, J. A., Platten, S. M., and Monselesan, D.: Projection of subtropical
1721 gyre circulation and associated sea level changes in the Pacific based on CMIP3
1722 climate models. *Clim. Dyn.*, 43, 131-144, <https://doi.org/10.1007/s00382-013-1902->
1723 [x](#), 2014.
1724

设置了格式: 字体: 倾斜

